PONTIFICIA UNIVERSIDAD CATOLICA DE CHILE

ESCUELA DE INGENIERIA

STATES OF STRESS AND SLIP PARTITIONING WITHIN A CONTINENTAL STRIKE-SLIP DUPLEX AND THEIR TECTONIC AND MAGMATIC SIGNIFICANCE

PABLO CRISTIÁN ITURRIETA

Thesis submitted to the Office of Research and Graduate Studies in partial fulfillment of the requirements for the Degree of Master of Science in Engineering

Advisors:

JOSÉ CEMBRANO P.

DANIEL HURTADO S.

Santiago de Chile (July, 2017)

PONTIFICIA UNIVERSIDAD CATOLICA DE CHILE

ESCUELA DE INGENIERIA

STATES OF STRESS AND SLIP PARTITIONING WITHIN A CONTINENTAL STRIKE-SLIP DUPLEX AND THEIR TECTONIC AND MAGMATIC SIGNIFICANCE

PABLO CRISTIÁN ITURRIETA

Members of the Committee

JOSÉ CEMBRANO P.

DANIEL HURTADO S.

GONZALO YAÑEZ C.

PABLO SALAZAR R.

JUAN CARLOS HERRERA M.

Thesis submitted to the Office of Research and Graduate Studies in partial fulfillment of the requirements for the Degree of Master of Science in Engineering

Santiago de Chile (July, 2017)

Si existo, en la búsqueda me pierdo
y si acaso me encuentro
es porque a ti, mar, regreso
llevando más de un solo recuerdo

ACKNOWLEDGMENTS

This work is dedicated to my mother, Norma, to whom I owe everything that I have become. Also to my father, whose support and caring aided me through this never-ending youth. To José, I cannot thank you enough for all that you have taught me, whether your passion for science, the love for small details of nature (i.e. weather) or large numbers estimate. To Daniel, for your endless patience and for putting your faith in me, in a time when not many others would.

I would like to say thanks to Gomila, Tomás, Tiaren, Ashley, Pame and Felipe(s), whose persistent calls for procrastination gave me joy every day in the office. Mariel, thank you for everything, especially for saving me numerous occasions from my own disaster. Also, thanks to Blocky for your absurdness and non-sense fun throughout this time. Thanks to my friends of Chiloé, who have always passed by the capital encouraging me to keep the hard work. To Betty, to whom I miss dearly. Finally, I would like to thank my little brothers, given that I have probably learned more from them than backwards, and my Tía Marcela, Tita y Mamilú for taking care of me all of this time.

This research was supported by projects FONDECYT n°1141139 and FONDAP n°15090013 "*Centro de Excelencia en Geotermia de los Andes*" (CEGA).

GENERAL INDEX

LIST OF TABLES

TABLE OF FIGURES

RESUMEN

Los cinturones orogénicos en márgenes de subducción oblicuos acomodan la deformación en varios dominios paralelos a la fosa, comúnmente sosteniendo la componente de rumbo paralela a la fosa de la convergencia. Sin embargo, el estado de stress y la cinemática de los arcos volcánicos es más compleja de lo usualmente reconocido, incluyendo fallas de primer- y segundo-orden con sentidos de deslizamiento característicos e interacción mutua entre ellas. Estas fallas son usualmente organizadas en dúplex de rumbo de escala regional, asociados con deformación heterogénea de largo y corto plazo, así como con actividad magmática. Este es el caso del Sistema de Falla Liquiñe-Ofqui, con una extensión de 1100 km en los Andes del Sur, constituido de dos fallas maestras superpuestas y paralelas al margen, unidas por varias fallas secundarias de rumbo NE. En este trabajo, presentamos un modelo de Elementos Finitos para caracterizar la naturaleza y distribución espacial del stress a través y a lo largo del arco volcánico en los Andes del Sur, con tal de entender la partición del deslizamiento y la conexión entre tectónica y magmatismo, particularmente durante la fase intersísmica del ciclo sísmico de subducción. Correlacionamos la dinámica del dúplex de rumbo con evidencia geológica, sísmica y transporte de magma documentada por trabajos previos, mostrando consistencia entre el modelo y el comportamiento inferido del sistema de falla. Nuestros resultados muestran que la orientación del máximo stress principal es heterogéneamente distribuida en el margen continental, variando entre 15° y 25° antihorario (con respecto al vector de convergencia) en las fallas maestras y 10° a 19° horario en los dominios del antearco y trasarco. Calculamos la elipticidad del tensor de stress, indicando cizalle simple en la falla maestra este y stress transpresivo en la falla maestra Este. Las fallas subsidiarias son sometidas a un estado de stress extensivo-a-transtensivo. La falla maestra Este muestra tasas de deslizamiento de 5 a 10mm/año, mientras que las fallas maestra Oeste y subsidiarias muestran tasas de 1 a 5mm/yr. Nuestros resultados indican que las fallas subsidiarias favorablemente orientadas sirven como conductos de magma, particularmente donde se

encuentran cerca de una intersección con una falla maestra. También, el deslizamiento de un segmento de falla es potenciado cuando la cinemática de una falla adyacente es superpuesta a la carga tectónica regional. De esta manera, los modelos de Elementos Finitos ayudan a comprender el fenómeno acoplado de tectónica y procesos volcánicos, demostrando que las observaciones geológicas y geofísicas pueden ser descritas por un pequeño número de condiciones de borde claves.

ABSTRACT

Orogenic belts at oblique convergent margins accommodate deformation in several trench-parallel domains, one of which is the magmatic arc, commonly assumed to take up the margin-parallel, strike-slip component. However, the stress state and kinematics of volcanic arcs is more complex than usually recognized, involving first-and second-order faults with distinctive slip directions and mutual interaction. These are commonly organized into regional scale strike-slip duplexes, associated with both long-term and short-term heterogeneous deformation and magmatic activity. This is the case of the 1100 km-long Liquiñe–Ofqui Fault System in the Southern Andes, made up of two overlapping margin-parallel master faults joined by several NE-striking second-order faults. In this work, we present a finite element model to study the nature and spatial distribution of stress across and along the volcanic arc in the Southern Andes to understand slip partitioning and the connection between tectonics and magmatism, particularly during the interseismic phase of the subduction earthquake cycle. We correlate the dynamics of the strike-slip duplex with geological, seismic and magma transport evidence documented by previous work, showing consistency between the model and the inferred fault system behavior. Our results show that maximum principal stress orientations are heterogeneously distributed within the continental margin, ranging from 15° to 25° counter-clockwise (with respect to the convergence vector) in the master faults and 10–19° clockwise in the forearc and backarc domains. We calculate the stress tensor ellipticity, indicating simple shearing in the eastern master fault and transpressional stress in the western master fault. Subsidiary faults undergo transtensional-to-extensional stress states. The eastern master fault displays slip rates of 5 to 10 mm/yr, whereas the western and subsidiary faults show slips rates of 1 to 5 mm/yr. Our results endorse that favorably oriented subsidiary faults serve as magma pathways, particularly where they are close to the intersection with a master fault. Also, the slip of a fault segment is enhanced when an adjacent fault kinematics is superimposed on the regional tectonic loading. Hence, finite

element models help to understand coupled tectonics and volcanic processes, demonstrating that geological and geophysical observations can be accounted for by a small number of key first order boundary conditions.

1. INTRODUCTION

The dynamics of tectonic plates in the Earth's exterior generates most of the geological processes we can currently observe. These processes include the building of mountain ranges (orogenesis), earthquakes, volcanism and fluid circulation throughout the crust in general, which implies hydrothermal activity and ore deposits formation. However, the extent of the Plate Tectonics theory, which has been the geoscientist paradigm since the early 60's, remains to be grasped. In this context, advances in fracture and continuum mechanics theories of solid media can contribute to improve our understanding of the Earth tectonics as a complex and transient system, while developing a theoretical framework upon which we can firmly build our qualitative knowledge.

Andean tectonics is controlled by the subduction and convergence between the Nazca and South American plates. It is an active margin upon which Chile is located. Its susceptibility to earthquake hazard is not only of subduction nature, but also related to crustal deformation. The latter has been associated with volcanic activity (e.g. Lara et al., 2008; Legrand et al., 2011; Wicks et al., 2011), therefore, understanding the interplay between both is essential to provide a rigorous hazard analysis of the region.

This thesis addresses the nature of the relationship between regional tectonics, crustal faulting and magma transport through the Earth's crust using a non-linear mechanics approach, and its associated numerical solution by means of the finite element method. First, I introduce the reader to basic concepts of geological and tectonic processes. After, I state the scientific problem, its significance, the objectives and the hypothesis, upon which this work is based. Consequently, a detailed review of the methodology is provided. The development and outcome of this research are presented in chapter 2, which contains the manuscript named *States of stress and slip partitioning within a continental strike-slip duplex: tectonic and magmatic implications by means of finite element modeling*, already published in the journal *Earth and Planetary Science Letters*.

1.1 Basic geological concepts

1.1.1 Faults, their geometry and kinematics

In geology, a fault is a tabular volume found in a rock mass, whose adjacent blocks have been relatively displaced. Some faults are as thin as a few millimeters and can be approximated as a discrete surface. Other faults constitute a tabular object of larger volume, reaching widths of hundreds of meters (Faulkner et al., 2010). Most faults in nature can be assimilated to a plane rather than a curved surface. Therefore, fault geometry (Figure 1-1) can be defined in space by two angles, strike (ρ) and dip (μ), using the North and the horizontal plane as a reference system. The rock block above the fault plane is named hanging-wall and the block beneath is called foot-wall. Alternatively, the fault is defined by a unique normal vector ($\hat{\boldsymbol{n}}$). The fault's relative displacement is characterized by a slip vector ($\hat{\boldsymbol{s}}$), whereas the null axis, where no deformation exists, is denoted as the $\hat{\boldsymbol{b}}$ axis. The plane where the entire slip, and hence deformation, localizes is called the movement plane.

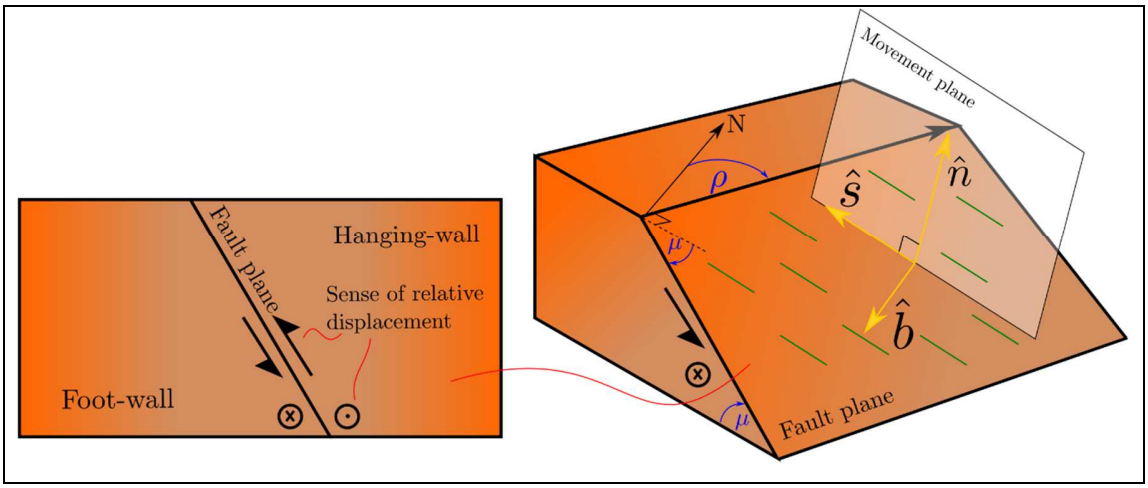

Figure 1-1: Geometrical description of a simplified fault.

The fault sense of displacement, hereafter loosely referred as kinematics, is grouped into four end members: (a) normal fault, which implies a dip-parallel displacement and a descending hanging-wall; (b) reverse fault, also dip-parallel, but where the hanging wall ascends; (c) dextral fault, where the displacement is restricted to the strike and the right block moves towards a standing observer; (d) sinistral fault, same as the former, except the left block moves towards the observer. Combined kinematics are defined as oblique faults and named after the combination of the composing kinematics (e.g. normal-dextral).

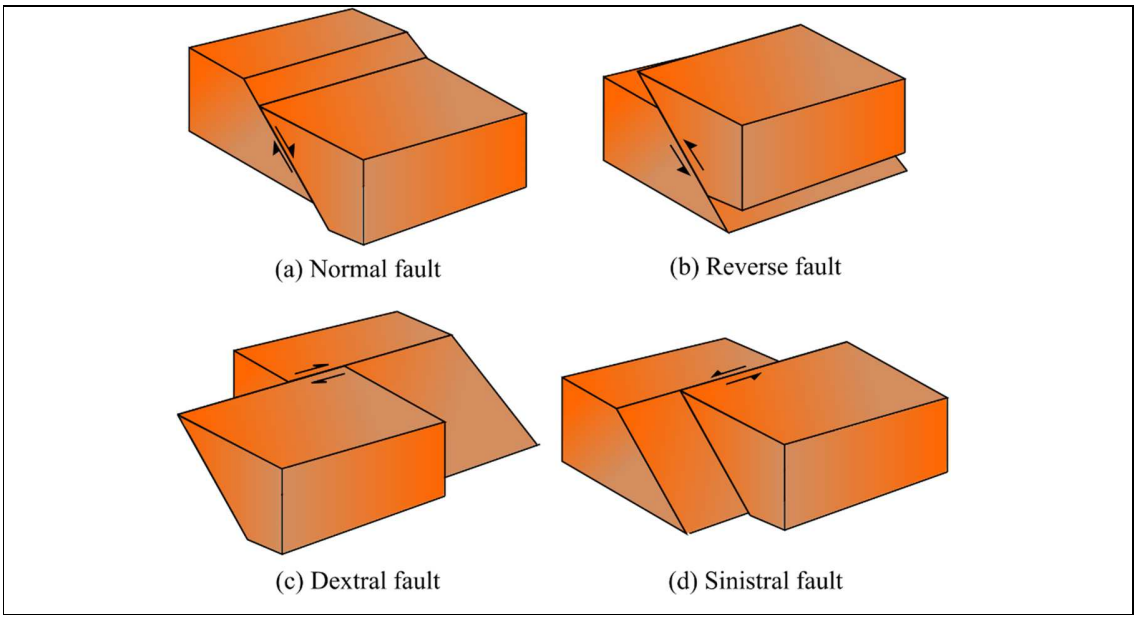

Figure 1-2: End-members of a fault's kinematics. Arrows indicate the relative sense of slip.

1.1.1 Faults, earthquakes and deformation

When brittle faulting occurs, the dissipation of potential elastic energy is attained through a nearly instantaneous slip, which perturbs the elastic medium generating the propagation of mechanical waves, a phenomenon known as earthquake. Whereas the earthquake's wave propagation can be modeled by a complex system of hyperbolic partial differential equations, the permanent deformation of the fault-slip can be approximated by means of

continuum mechanics. Such approach is usually performed by seismologists to understand the short-term behavior of a fault (e.g. subduction earthquakes), whereas permanent deformation of the crust is of interest to structural geologists and tectonicists.

Let Ω_0 be the reference configuration of any undeformed body, see Figure 1-3. Once deformation occurs, the body can be translated, rotated and distorted into a deformed configuration Ω_f. A point that belongs to Ω_0 is generically described by the vector $\boldsymbol{X}$ in a standard basis $\boldsymbol{e_1} - \boldsymbol{e_2} - \boldsymbol{e_3}$, whereas the same point in the deformed configuration is described by $\boldsymbol{x}$. The injective function that relates a given $\boldsymbol{X}$ to its corresponding $\boldsymbol{x}$ is defined as the deformation mapping $\boldsymbol{\varphi}(\boldsymbol{X})$. Further, we can define the displacement field as $\boldsymbol{u}(\boldsymbol{X}) = \boldsymbol{\varphi}(\boldsymbol{X}) - \boldsymbol{X} = \boldsymbol{x} - \boldsymbol{X}$.

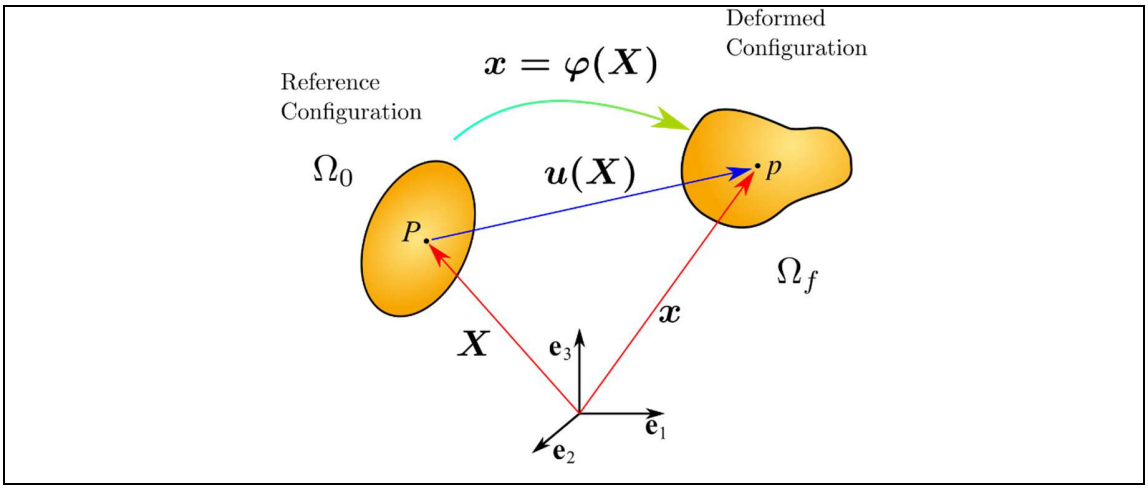

Figure 1-3: Schematic description of deformation.

It is of our interest to quantify the distortion of the solid associated to deformation, neglecting its rigid body motion. In the following, distortion will be referred to as strain. Hence, we want to relate the vector $\delta\boldsymbol{X}$, which defines the relative position between $\boldsymbol{X}$ and any point of its vicinity, and the vector $\delta\boldsymbol{x}$. Let $\nabla(\cdot)$ the gradient operator. Then, we define the gradient of the displacement field, which is a second-order tensor, as:

$$\nabla \boldsymbol{u} = \frac{\delta \boldsymbol{x} - \delta \boldsymbol{X}}{\delta \boldsymbol{X}} = \frac{\delta \boldsymbol{u}}{\delta \boldsymbol{X}} = \frac{\delta u_i}{\delta X_j} = \begin{bmatrix} \frac{\delta u_1}{\delta X_1} & \frac{\delta u_1}{\delta X_2} & \frac{\delta u_1}{\delta X_3} \\ \frac{\delta u_2}{\delta X_1} & \frac{\delta u_2}{\delta X_2} & \frac{\delta u_2}{\delta X_3} \\ \frac{\delta u_3}{\delta X_1} & \frac{\delta u_3}{\delta X_2} & \frac{\delta u_3}{\delta X_3} \end{bmatrix} \quad \textbf{Equation 1-1}$$

Where i, j denotes the indices of the vectors. Assuming that the magnitude of the displacement field and displacement gradient tensor are small, we study strain by means of the infinitesimal strain tensor, which takes the form:

$$\boldsymbol{\varepsilon} = \frac{1}{2}(\nabla \boldsymbol{u} + \nabla \boldsymbol{u}^t) \quad \textbf{Equation 1-2}$$

The infinitesimal strain tensor defines the stretching and shear distortion of any given point in the reference configuration. With this concepts at hand, we derive the displacement gradient tensor by homogenizing the discrete deformation of faulting into a continuum framework (Molnar, 1983), as shown in Figure 1-4. Let us consider an infinitesimal volume, which is deformed by faulting. The equivalent deformed continuum body preserves the original volume and requires the same strain energy to deform. Therefore, the components $\delta u_i / \delta X_j$ of the gradient tensor can be related to the components of the unit slip vector $\hat{\boldsymbol{s}}$ and the fault plane normal $\hat{\boldsymbol{n}}$

$$\nabla \boldsymbol{u} = \frac{M_g}{V} s_i n_j = \frac{M_g}{V} \begin{bmatrix} \hat{s}_1 \\ \hat{s}_2 \\ \hat{s}_3 \end{bmatrix} [\hat{n}_1 \quad \hat{n}_2 \quad \hat{n}_3] = \frac{M_g}{V} \hat{s} \otimes \hat{n} \quad \textbf{Equation 1-3}$$

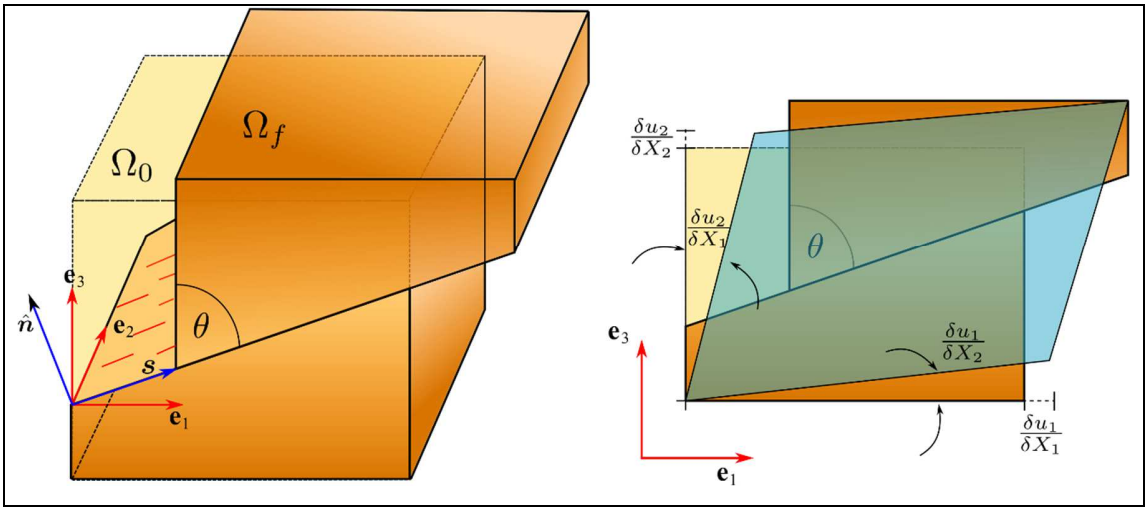

Figure 1-4: Homogenization of discrete deformation produced by faulting. We conveniently chose a vector basis where e_2 coincides with the null axis $\hat{b}$. Given that there is no deformation involved in the latter, we can provide a simplified homogenization in the $e_1 - e_3$ plane.

Where V is the infinitesimal volume considered, $M_g = A|\boldsymbol{s}|$ the geometric seismic moment, A the fault plane area, $|\boldsymbol{s}|$ the magnitude of the slip and $\otimes$ is the dyadic tensor product. With these definitions, the infinitesimal strain tensor (defined in Equation 1-2) takes the form:

$$\boldsymbol{\varepsilon} = \frac{M_g}{2V}(\hat{s} \otimes \hat{n} + \hat{n} \otimes \hat{s}) \qquad \textbf{Equation 1-4}$$

In structural geology practice, it is difficult to estimate the fault plane area and the deformed volume. However, if we neglect the strain magnitudes, the directions of maximum extension $\hat{\boldsymbol{t}}$, null deformation axis $\hat{\boldsymbol{b}}$ and maximum shortening $\hat{\boldsymbol{p}}$ can still be calculated from computing the eigenvectors of $\boldsymbol{\varepsilon}$, ordered from the maximum to the minimum corresponding eigenvalues, respectively. The principal axes then define the entire kinematics of a fault, or as done in seismology, define the fault where an earthquake is nucleated.

The orientations of the infinitesimal strain tensor can be represented through a graphical tool, named focal mechanism solution (Figure 1-5), which is commonly used in seismology to describe the kinematics of an earthquake. The fault plane and all the extension and shortening directions are plotted in a stereographic-net (Schmidt net), which represents every possible orientation in space, according to their azimuth $\boldsymbol{\delta}$ and plunge $\boldsymbol{\beta}$. It is a two-dimensional projection of a 3D geometry, usually planes and lines. Therefore, planes are represented as curves and lines as dots. The focal mechanism solution depicts the maximum extension axis $\hat{\boldsymbol{p}}$ and maximum shortening $\hat{\boldsymbol{t}}$, whereas all the extension directions are colored and the shortening directions are left in white. The plane that contains both the fault plane normal and the null axis is referred as the conjugate plane. Physically, it represents the only alternative fault plane solution to the strain tensor plotted.

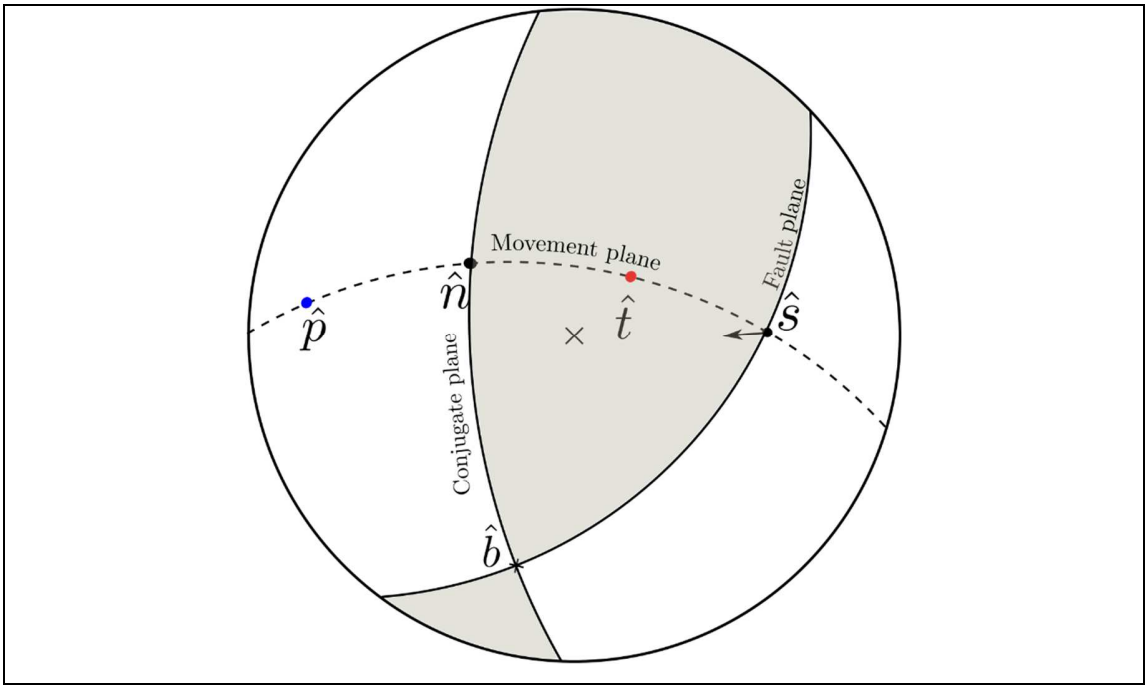

Figure 1-5: Focal mechanism solution plotted on a stereographic net. Filled dihedra represent all the directions where extension exists, whereas the white dihedra represents shortening. In the plot, fault plane elements are represented, such as the fault plane itself, its normal vector $\hat{n}$, the slip vector $\hat{s}$ and the null axis $\hat{b}$.

Therefore, using focal mechanism solutions, we can graphically illustrate the end members of the possible fault's kinematics (Figure 1-2) as shown in Figure 1-6.

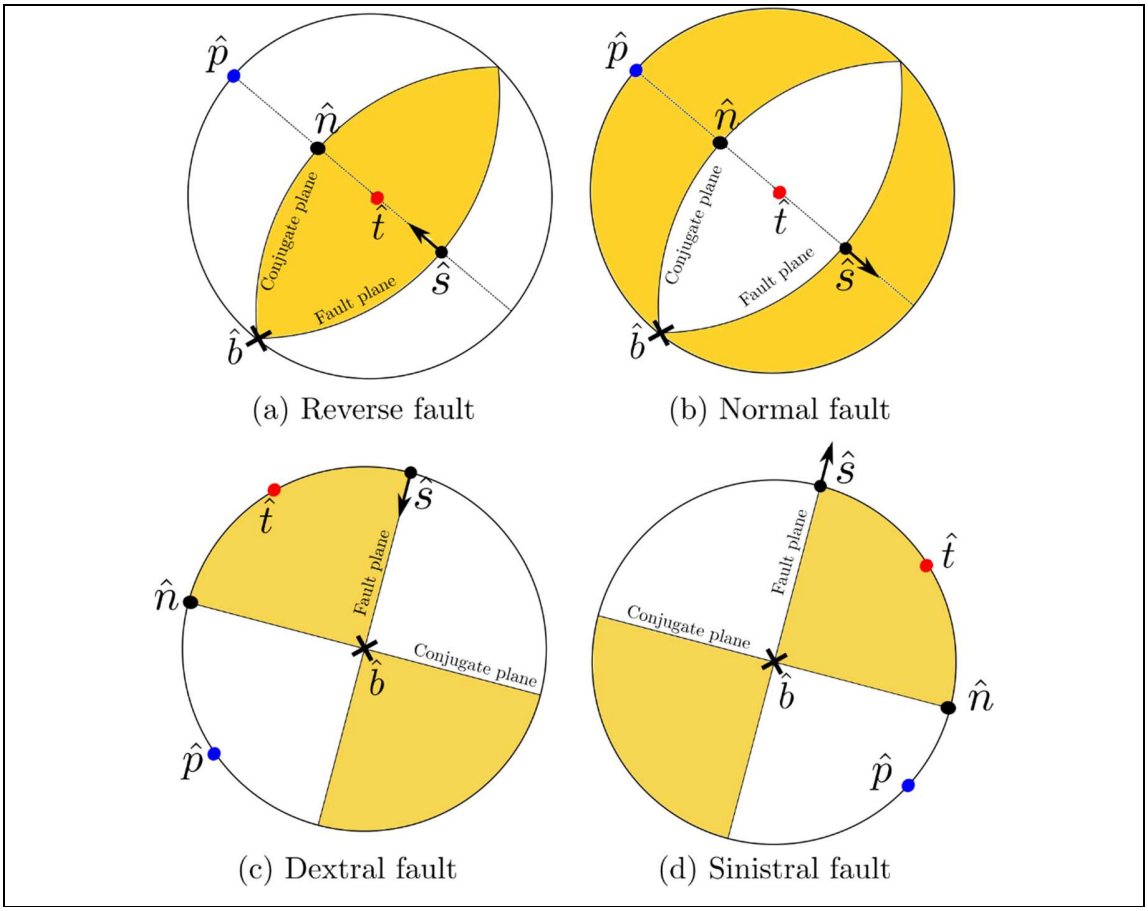

Figure 1-6: Focal mechanism solutions for each of fault kinematics end members.

1.1.2 Anatomy and rheology of a transcurrent fault zone at depth

As depth increases in Earth, so does temperature. The temperature gradient is controlled by the heat input at its base from the asthenosphere, the rock's composition, magma conduits and reservoirs, the decay of radioactive elements present within rocks, among others (e.g. Chapman, 1986). Moreover, transcurrent faults are large strike-fault systems composed of several faults of similar nature, which may crosscut the continental

lithosphere. They can serve as magma conduits, at least in the crust (e.g. K Nakamura, 1977; Rubin, 1995) and upper mantle (e.g. D. Hutton, 1988) and are usually spatially associated with the volcanic arc. The potentially anomalous thermal gradient in a fault system activates different deformation mechanisms through depth, allowing for deformation to localize in a shear zone. Three main domains are identified through depth in the anatomy of a transcurrent fault zone, whose rheology depends in distinct parameters. Following, we define this domains in terms of their geometry and stress-strain relation.

(a) *Brittle domain of the lithosphere*

Brittle behavior of rocks is limited to a region encompassing the near surface down to a few kilometers beneath (1~10km). Brittle faults are tabular volumes, in which the rock is deformed through the slide of its composing grains, along with their rotation and comminution (Scholz, 2002). However, at a regional scale, brittle faults can be simplified as surfaces or planes, given that the width of a brittle fault damage zone commonly reach up to only tens of meters.

The brittle failure of rocks is well studied by rock mechanics, and usually implies a pressure-dependent rock's strength, which is function of the rock's cohesion (c) and friction coefficient (ϕ). The rock's strength is commonly described by the Mohr-Coulomb equation:

$$\tau_{crit} = c + \sigma_n \tan\phi \qquad \textbf{Equation } 1\text{-}5$$

where τ_{crit} is the rock shear strength or yield stress and σ_n is the normal stress on a given plane. This gives a linear relation between the strength of the rock and the depth considered. Furthermore, the presence of fluids within the fault zone decreases the normal stress at which the rock is subjected (e.g. Hubbert & Rubey, 1959; Secor, 1965). This

implies that the strength of the rock decreases considerably when hydrothermal fluids or magma is contained within them.

Brittle faults are commonly interconnected between a series of main and subsidiary faults, thus defining a fault zone. Riedel, (1929) provided a descriptive framework of the geometric relation between a main fault plane and its subsidiary faults in cohesive and non-cohesive granular materials, as shown in Figure 1-7. This geometric model remains valid until today, and it has been proved that self-similarity exists between different observation scales (Jensen et al., 2011; Tchalenko, 1970). Most of these secondary structures can often be seen in the field.

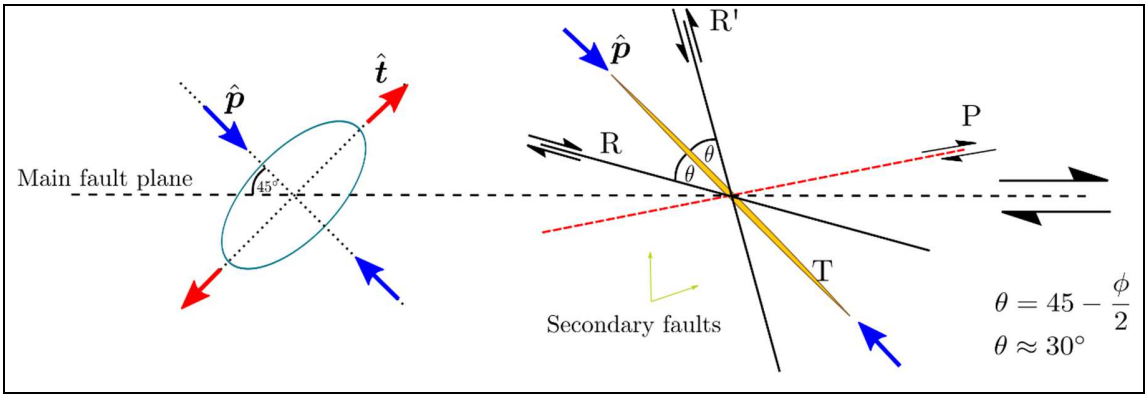

Figure 1-7: Riedel model of fracturing. Secondary fractures R, R' and P are usually shear fractures, whereas T fractures describes tension gashes, which are usually infilled with precipitated hydro-thermal or magmatic fluids. Also, the infinitesimal strain tensor principal directions are plotted

(b) *Brittle-plastic transition*

Crystal-plastic deformation mechanisms are onset where a critical activation energy and temperature are exceeded. This occurs when at least one of the minerals composing the rock exceeds first the plasticity limit, which is usually quartz in granitic rocks, while the remaining minerals behave in a brittle fashion. The crustal domain where

both brittle and plastic deformation co-exist is defined as the brittle-plastic transition, whose location is defined by the thermal gradient of the lithosphere. In transcurrent fault systems associated with volcanic arcs the brittle-plastic depth is $\approx 10-15\,\mathrm{km}$ (e.g. Scholz, 1988).

Here, the rheology is controlled by dislocation creep, in which glide and climb of dislocations occurs within a crystal lattice (e.g. Tullis & Yund, 1987), micro-fracturing networks and fluid-pressure solution, which is the dissolution of the grain boundaries where stress is concentrated in the grain contact interface. Deformation is commonly localized in cm-to-m width plastic shear bands, whereas in its edges, filled microfractures can be found (e.g. Segall & Simpson, 1986). Moreover, it is proposed that this brittle behavior causes the nucleation of earthquakes within the first kilometers of the brittle-plastic transition (Scholz, 1988).

One of the proposed rock strength to model the brittle-plastic transition, with particular attention to dislocation glide, is the Peierls stress-strain law (Regenauer-Lieb & Yuen, 2003b). It defines the yield stress of a rock in terms of the strain rate $\dot{\varepsilon}$, the initial yield stress τ_0, the ultimate yield stress τ_∞, the Elastic modulus E, the water pressure p and the water influence exponential ratio α:

$$\tau_{crit} = \tau_\infty - \tau_\infty \sqrt{\left(-\frac{RT}{Q+pV}\right)\ln\left(\frac{\dot{\varepsilon}}{\alpha E \tau_0}\right)}, \qquad \dot{\varepsilon} \geq E\tau_0 \qquad \textbf{Equation 1-6}$$

Where T is the rock's temperature, and Q and V is the activation energy and volume respectively. However, an approximation is given by the von-Mises criterion and the Voce's hardening law (Regenauer-Lieb et al., 2004; Schmalholz & Maeder, 2012a) when we neglect the influence of the water and assume a steady-state strain loading and a constant thermodynamic state. Thus, the rock's strength depends on the accumulated plastic strain $\underline{\varepsilon}^p$, which is modeled through the expression:

$$\tau_{crit} = \tau_{\infty} + (\tau_0 - \tau_{\infty})\exp(-\beta\underline{\varepsilon}^{p}), \qquad \textbf{Equation 1-7}$$

where β is a hardening exponential rate, which define the asymptotic behavior of the stress-strain curve, also known as creeping parameter.

(c) *Plastic-viscous domain of the lithosphere*

At deeper structural levels (> 30 km), rocks behave like a fluid of large viscosity (Carter, 1976). Fault zone widens and spreads into several discrete deformation bands. The mechanisms that control the rock's rheology are: pressure solution; volume diffusion (Nabarro-Herring creep) and grain boundary diffusion (Coble's creep) (e.g. McClay, 1977). Several power-laws have been defined to characterize the stress-strain relationship, according to a specific deformation mechanism, which are beyond the scope of this manuscript. The rheology domains that comprises a transcurrent fault system and their approximate strength vs. depth are illustrated in Figure 1-8.

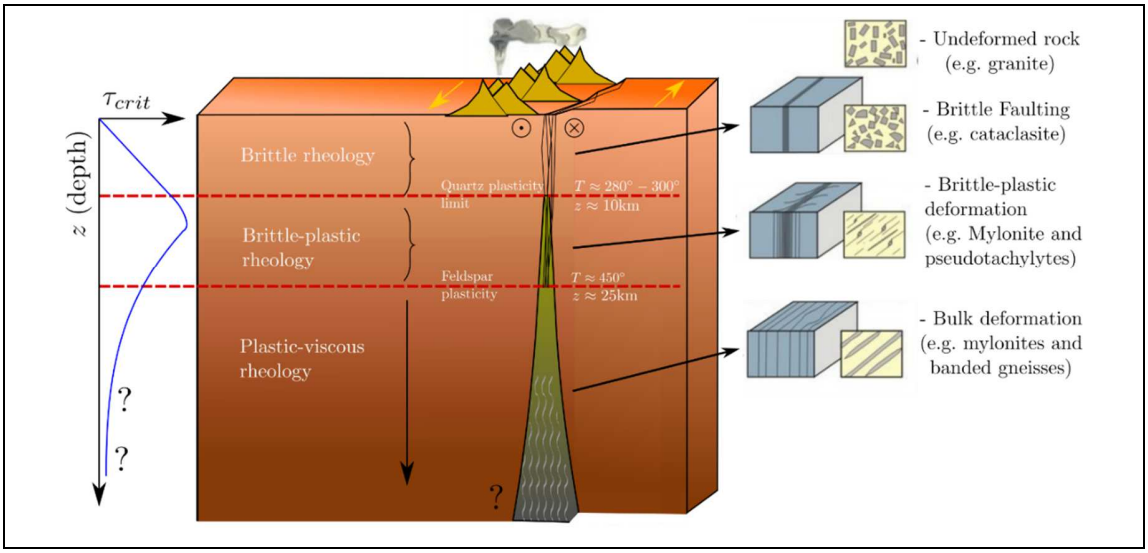

Figure 1-8: Anatomy of a transcurrent fault in depth, and its failure strength profile, modified from Scholz, (1988). Question marks defines those domains whose exact geometry remain unconstrained.

1.1.3 States of stress: The stress tensor ellipticity and orientation

The stress tensor $\boldsymbol{\sigma}$ can be entirely described by its three eigenvectors and eigenvalues. However, knowing the exact magnitudes in tectonics may be a difficult task to perform. Some approximations can be provided by a data conjunction of boreholes breakouts (e.g. Zoback & Healy, 1992), focal mechanisms, hydro-fracturing and geological indicators, which are grouped in a world stress map (e.g. Heidbach et al., 2010). However, these approximations have a great uncertainty due to its large resolution and neglects the large stress heterogeneity within the crust domains.

In this regard, a fair approximation of the stress orientations and relative magnitudes can be provided by numerical modeling, which is the approach of this work. It is important to keep in mind that these orientations are related, but not equal, to strain eigenvectors, even if such regimes are named the same. A compressional state is attained where both σ_1 and σ_2 are horizontal, whereas an extensional state where σ_1 is vertical. Strike-slip states of stress occurs where σ_1 and σ_3 are in a horizontal plane. Orientation end-member scenarios are illustrated in Figure 1-9, however, an oblique stress tensor is also possible.

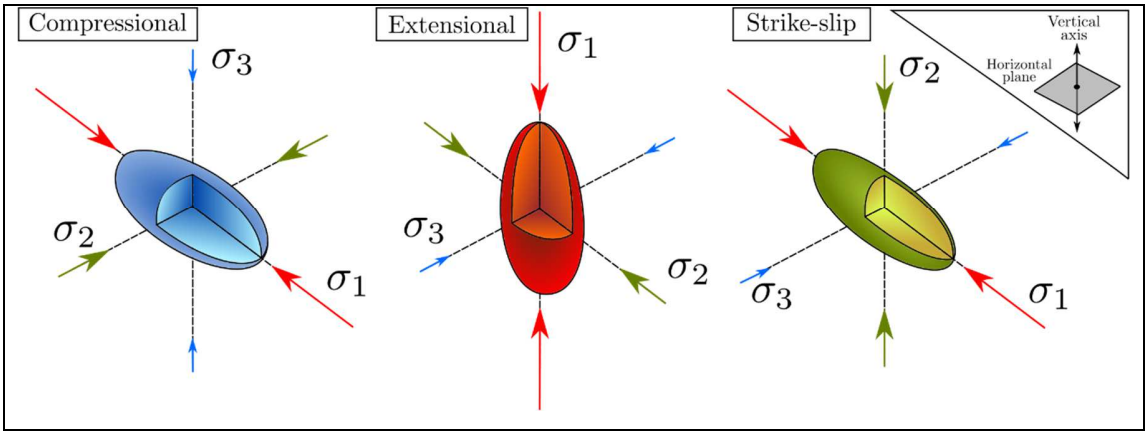

Figure 1-9: States of stress with their associated stress ellipsoid. The axes of the ellipsoid illustrate the relative magnitudes between stresses.

By definition, transcurrent fault systems undergo an overall strike-slip state of stress. Since that they are often located within a convergent margin, the compressive component of convergence is sustained by both the fore-arc (the portion of the continental lithosphere between the subduction margin and the volcanic arc – see Figure 1-15) and the back-arc (the lithosphere beyond the volcanic arc). The local state of stress of a transcurrent system is described by the relative magnitude of the principal stresses and the obliquity of the stress tensor to the fault zone. Thus, within a strike-slip state of stress, it is possible to define intermediate states, which range between the compressional and extensional states. These are called transtensional and transpressional, which are located either between pure-strike slip and extension or compression, respectively.

In this regard, we define the stress shape ratio (Ritz, 1994), which is the ellipticity of the stress tensor in terms of its eigenvalues. It is an adimensional parameter that defines the relative magnitudes between the principal stresses, therefore, indicating the position of σ_2 between σ_3 and σ_1 within the Mohr circle (Figure 1-10). Also, each state of stress in a fault zone has an associated deformation. Although the orientations of $\boldsymbol{\sigma}$ and $\boldsymbol{\varepsilon}$ are not necessarily parallel (due to anisotropy or non-associated plastic flow), they are located within the same octant of a Euclidean space, given that rocks are not an auxetic material ($\nu > 0$) and they follow the Drucker's postulate of stability ($d\boldsymbol{\sigma}: d\boldsymbol{\varepsilon} \geq 0$) in small deformations. Therefore, we can assume a fault zone loaded in a particular state of stress will deform in a similar fashion, which illustrated in Figure 1-10.

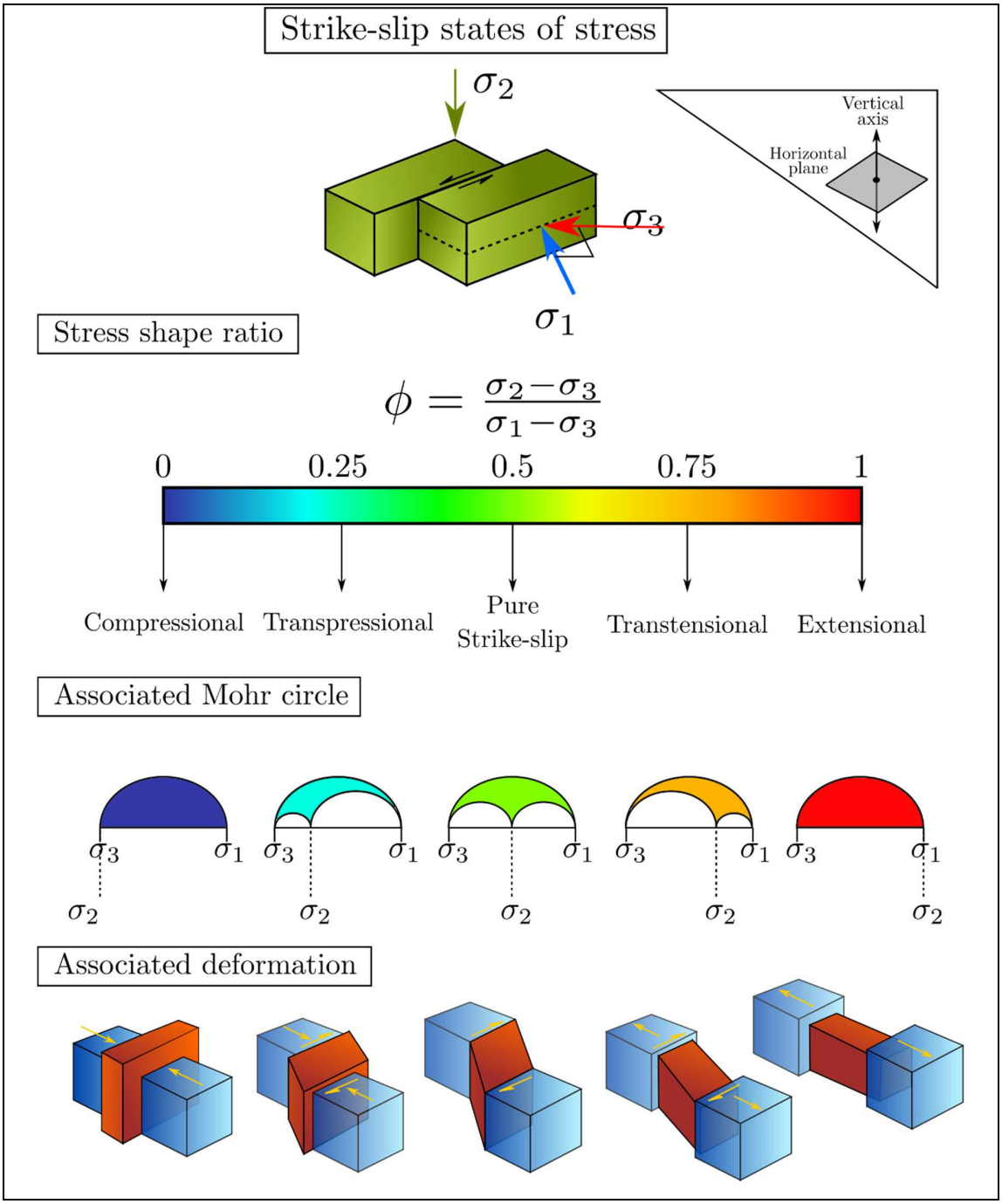

Figure 1-10: Strike-slip local states of stress. Their associated Mohr circle and deformation are illustrated for each case.

1.1.4 Fluid/magma transport and its relationship with states of stress

Magmatic and hydrothermal fluids are transported through brittle conduits in the lithosphere as is commonly described by Rock Mechanics. The link between fluid overpressure and the rock mechanical behavior (e.g. shear strength, slip) is highly complex, involving a coupled hydro-thermo-mechanical feedback. Fluid overpressure will decrease the effective normal stress, thus enhancing the probability of faulting, whereas faulting may produce local voids and a pressure decrease, which will produce a hydraulic gradient for fluid to flow (Sibson, 1992; Sibson & Moore, 1975)

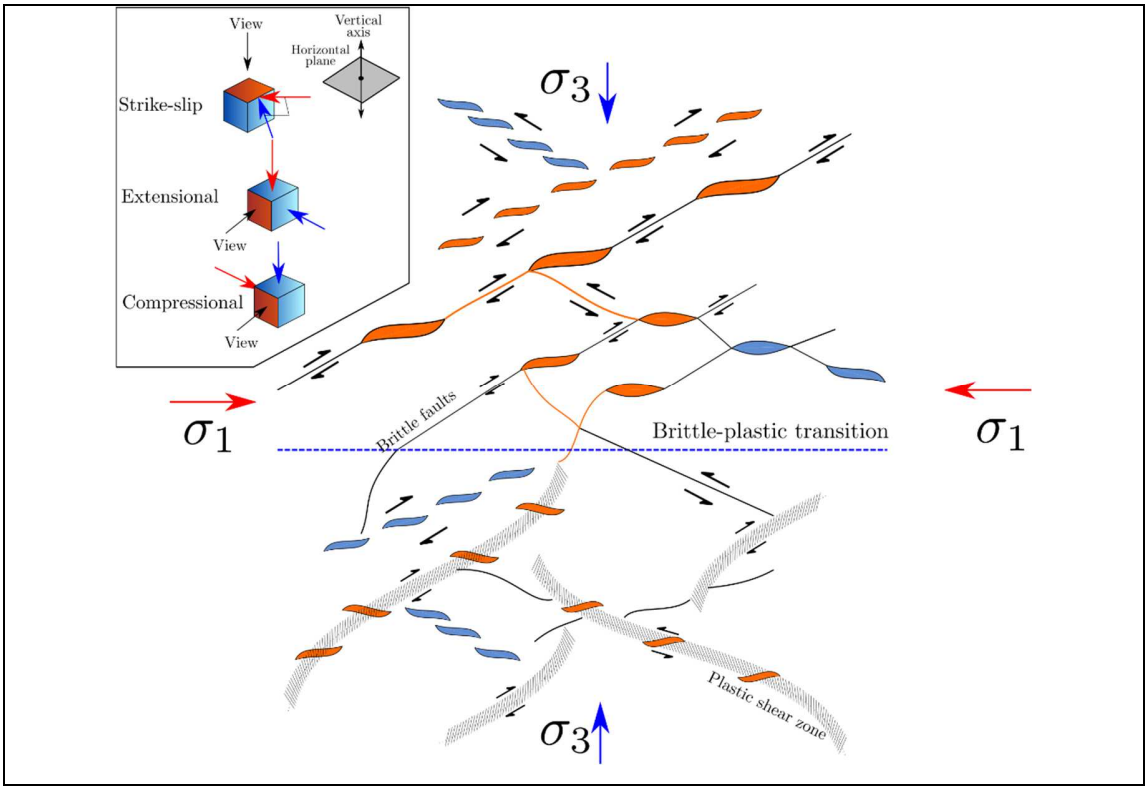

Figure 1-11: Sketch of fault-fracture networks associated with hydro-thermal and magmatic fluid transport conduits. Plane view of the figure is different for each state of stress, as shown in the box in the upper-left corner (modified from Sibson, (2004)).

Furthermore, the stress tensor orientation and relative magnitudes are related to fluid flow direction. In the brittle domain, compressional, extensional and strike-slip states of stress will create differently oriented fault-fracture networks (Figure 1-11). A compressional state of stress causes fault-fracture networks to orient sub-horizontally (e.g. Sibson, 1994, 2004), with low dip faults that transport fluids through the crust, whereas an extensional state of stress produces a vertical network. Strike-slip fault-fracture networks also are commonly vertical. Moreover, in the brittle-plastic domain, fault-fracture networks are spatially associated with plastic shear zones, in a similar fashion than the brittle domain, but rather in micro-fractures in the shear zones neighborhood.

To account for the relationship between stress tensor magnitudes and fluid transport, we define the fluid overpressure ratio (λ), which is the required combination of fluid overpressure P_f against lithostatic vertical stress σ_v upon which faulting with fluid transport occurs.

$$\lambda = \frac{P_f}{\sigma_v} \qquad \textbf{Equation 1-8}$$

When fluid flow occurs in the crust, it will require extensional fracturing (this refers to deformation, not to confuse with extensional state of stress) to ensure kinematic compatibility, whether it be through faulting, micro-cracks or grain boundaries. However, it is important to recognize that this can be achieved not only through an extensional state of stress, but rather requiring a different fluid overpressure value in every possible state. Whereas an extensional state of stress will require a lower pair of $\lambda - \tau$, strike-slip and compressional states will consequently require greater values. This is illustrated in the $\lambda - \tau$ diagrams (Cox, 2010; Roquer et al., 2017), as seen in Figure 1-12. Therefore, extensional and transtensional states of stress are the most optimal for fluid to flow within the crust.

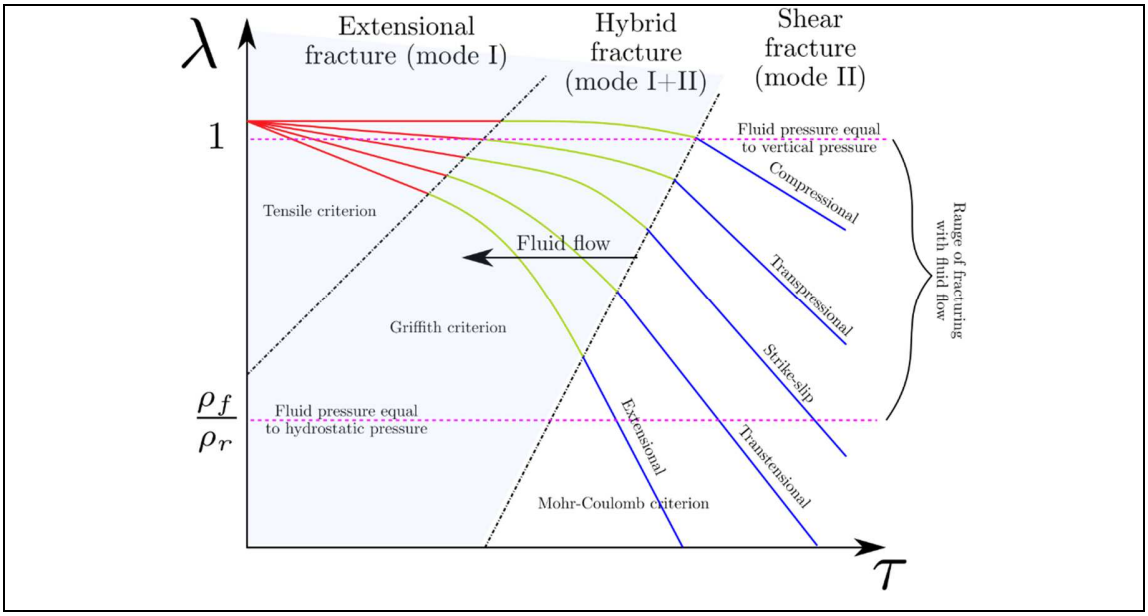

Figure 1-12: Schematic $\lambda - \sigma_v$ diagram, which indicates the required fluid/magma pressure and shear stress to fracture for each state of stress, at a given depth. Both extension fracturing (mode I) and hybrid (mode I+II) fracturing are described by the Tensile (in red) and Griffith criteria (in green), respectively. Pure shear fracturing (mode II) is described by the Mohr-Coulomb criterion (in blue). The range of λ where fracturing with fluid flow occurs, is between the lithostatic pressure ($\lambda = 1$) and the hydrostatic pressure of the fluid/magma ($\lambda = \rho_f/\rho_r$), where ρ_f is the fluid density and ρ_r is the density of the host rock. Fluid flow occurs within the extensional fracturing and hybrid fracturing (light blue region)

Furthermore, volcanic centers and their corresponding feeder dikes can also occur in any state of stress (Blanquat & Tikoff, 1998; Cembrano & Lara, 2009; Guineberteau & Bouchez, 1987; D. Hutton, 1988; D. H. . Hutton, 1982). However, in convergent margins they are commonly oriented sub-parallel to σ_1, in mode I fracturing as a response to tectonic local stress (Nakamura et al., 1977), as seen in Figure 1-13. Volcanic edifices and their flank vents are often aligned parallel to σ_1, and the shape of the flank vents (Tibaldi, 1995) is also elongated in this direction.

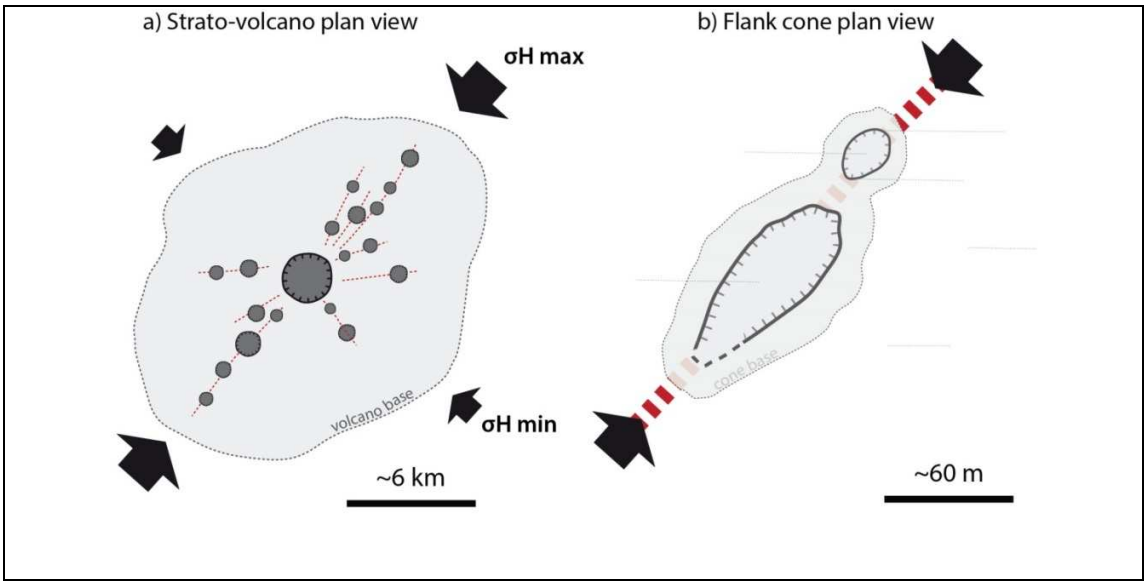

Figure 1-13: Traditional models of volcanic emplacement due to maximum horizontal stress. Modified after Nakamura, (1977); Tibaldi, (1995); Sielfeld. et al., (2016). In (a), Grey circles represent eruptive centers within a volcanic edifice. In (b), black lines represents the crater of these eruptive centers.

1.2 Tectonics of an obliquely convergent margin: The Andes Southern Volcanic Zone

The Andes Southern Volcanic Zone (SVZ) is tectonically controlled by the subduction and convergence between the Nazca plate and the South-America plate. The convergence velocity is 66mm/yr, with an obliquity of ~20° counter-clockwise with respect to the trench-orthogonal (Angermann et al., 1999). It has remained roughly the same for the past 10 million years (Argus et al., 2011; Kendrick et al., 2003). However, south of the Chile Triple Junction (between Nazca, South-America and Antarctica plates at 46° latitude in the continental margin), the convergence between the Antarctica and South-America plates is approximately orthogonal to the trench, with a velocity of 8mm/yr.

The obliquity of the convergence is sufficient for deformation and strain to partition within the continental crust (Arancibia et al., 1999; Cembrano & Lara, 2009; Pérez-Flores et al., 2016; Rosenau et al., 2006). The continental crust does not deform elastically, but instead,

the volcanic arc serves as a weak rheology domain, upon which most of the deformation localizes. It has been shown by numerous authors (Blanquat & Tikoff, 1998; Teyssier et al., 1995; Tikoff & Teyssier, 1994) that obliquely convergent margins commonly develop an intra-crust transcurrent fault system, which sustains a fraction, if not the whole, of the trench-parallel component of the convergence velocity. Both end-members of strain partitioning is shown in 1.2Figure 1-14.

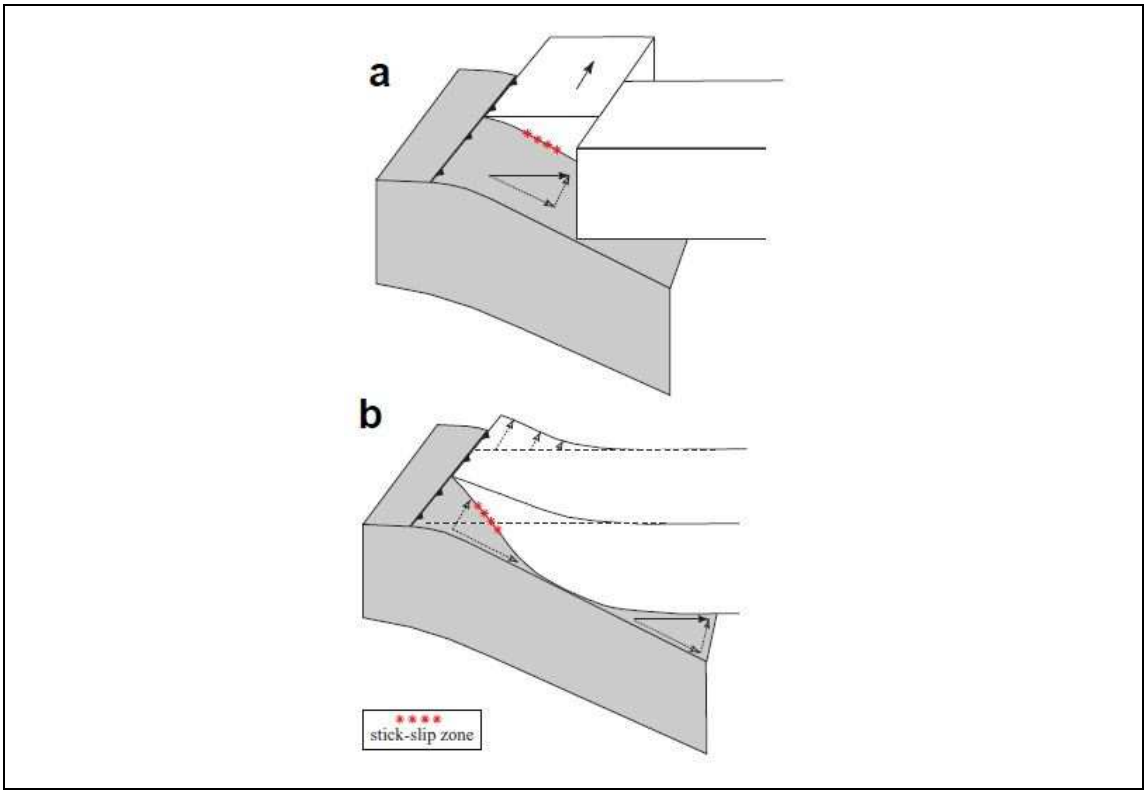

Figure 1-14: A schematic illustration of the end-members of strain partitioning within the continental crust. The red dots represent the stick-slip zone, which locks in the interseismic period of the subduction earthquake cycle. Convergence vector is decomposed into its trench-parallel and trench-orthogonal components. Scheme (a): shows a total strain partitioning in the continental crust, within which a forearc sliver develops. Scheme (b): the elastic strain is continuously distributed within the crust. In the earth, obliquely convergent margins can develop a strain partitioning in between these both end-members.

Furthermore, the zone where deformation is localized is far from being a discrete surface. The volcanic arc can reach up to hundreds of kilometers wide and consist of a series of anastomosed fault zones, which may serve as magma pathways from the mantle. The thermal anomaly caused by magmatic activity causes this zone to deform more easily and it is emplaced in the main cordillera of the Andes SVZ.

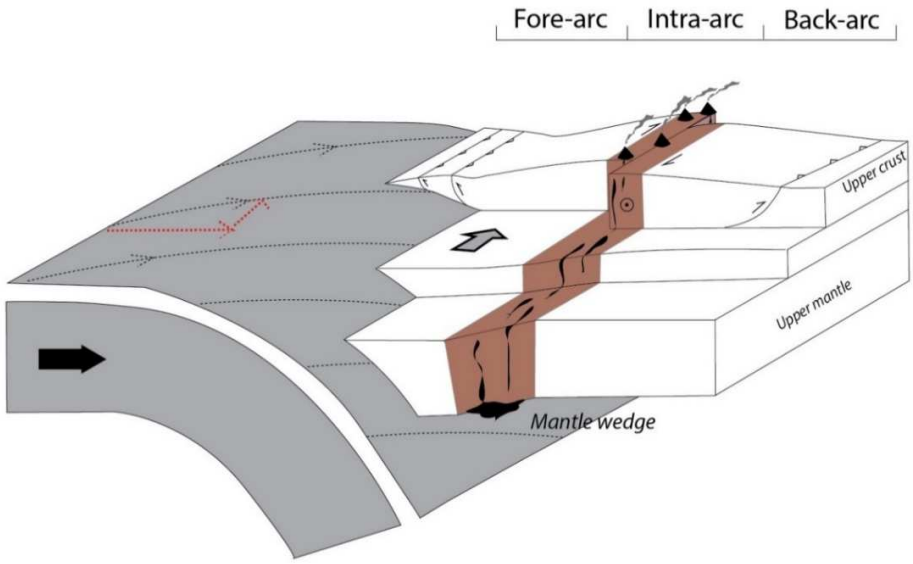

Figure 1-15: Illustration showing the geometry and kinematics of an obliquely convergent margin. The convergence vector can be decoupled into a trench-orthogonal component and a trench-parallel component, shown in red arrows. The trench-orthogonal component is accommodated at the plate's interface and at margin-parallel thrust faults at the fore-arc and back-arc regions. The trench-parallel component can be accommodated at trench-parallel strike-slip faults at the thermally weakened crust of the intra-arc. Modified after Blanquat & Tikoff, (1998) and Stanton-Yonge, (2016).

Deformation partitioning within the South-Andes margin, between 38°S and 47°S latitudes, is manifested through the Liquiñe-Ofqui Fault System (LOFS), which is an outstanding case study of a regional-scale transcurrent shear zone. It is a long lived intra-arc structure that has been active -at least- since 6 million years (José Cembrano et al., 2002). Geological evidence (e.g. G Arancibia et al., 1999; Lavenu & Cembrano, 1999),

along with seismic [Figure 1-16] (e.g. Lange et al., 2008; Legrand et al., 2011) and geodetic observations (Wang et al., 2007) documents its overall transpressional dextral kinematics.

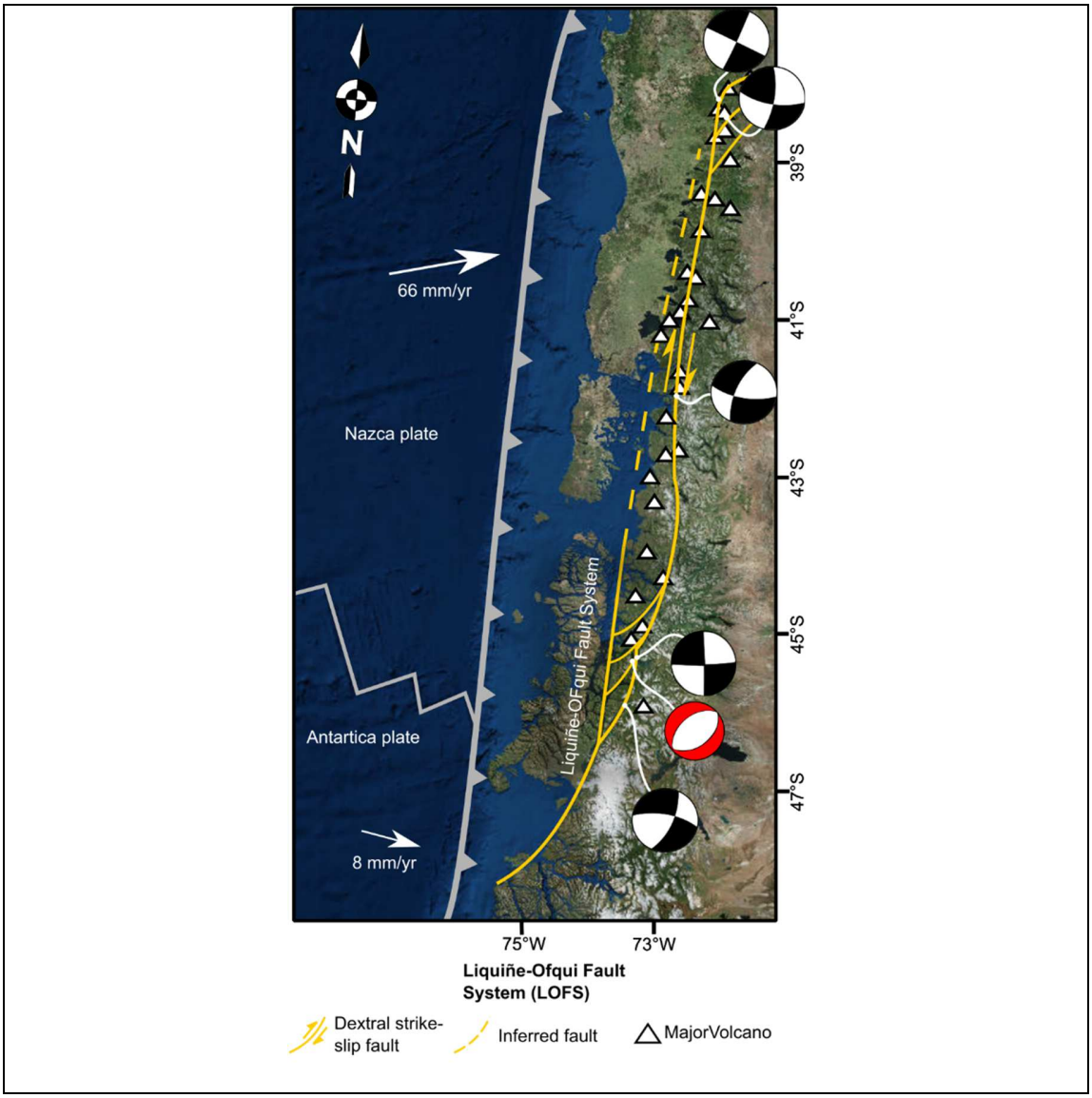

Figure 1-16: Tectonic setting showing the main fault strands of the LOFS within the South-Andean margin. Also, representative stratovolcanoes of the volcanic arc are shown in the figure. Main historic focal mechanism of the LOFS seismic activity are shown.

1.2.1 The Liquiñe-Ofqui Fault System (LOFS)

The architecture of a volcanic arc in an obliquely convergent margin is more complex than usually recognized. It is composed of several anastomosed faults, which mutually interact between each other and with secondary structures that splay off the main fault system. This crust weakness represented by a transcurrent fault system enables magma upward migration from the asthenosphere. However, different fault segments have unique styles of magmatism. Whereas extensional faulting involves a fast channel for magma to transport nearly uncontaminated by the crust itself, strike-slip to compressional faults are related to short, both in time and distance, pulses of magma transport, thus allowing the magma to pool in a reservoir, differentiating and contaminating with the host rock (e.g. Cembrano & Moreno, 1994). In this context, the LOFS is emplaced in the South-Andes volcanic arc itself. Its different fault segments undergo different states of stressing, thus allowing volcanism to manifest from different sources, from primitive to more evolved magmas (Cembrano & Lara, 2009). Several volcanic alignments can be found in major-to-secondary fault segments of the LOFS.

Furthermore, the LOFS is spatially related to sharp geomorphic lineaments, where faulting contributed to the landscape evolution by differential erosion (e.g. José Cembrano et al., 1996; Glasser & Ghiglione, 2009). High denudations rates, of nearly 1mm/yr in the South-Andes, are possible to the balance between transpressional surface uplift, post-glacial rebound and high glacial erosion rates (Thomson, 2002). Also, a largely documented hydrothermal activity has been documented on the LOFS entire extent. Active reservoirs are allowed to pool in the crust, with fault assisted reload and transport near to the surface (Lahsen, 1988; Tardani et al., 2016). This geothermal potential has been explored for the last century, with some attempts to produce electricity in large-scale power plants, which have not come to success (e.g. Sanchez-Alfaro et al., 2015). Furthermore, the architecture of these hydrothermal reservoirs have been documented by several authors, being composed of large fracture-vein networks, whose composition can depend on the fault

segment and structural level on which they are emplaced (Pérez-Flores et al., 2016; Roquer et al., 2017; Sánchez et al., 2013).

The LOFS displays two large NNE-striking master faults, which forms a strike-slip duplex (Figure 1-17) in the region of the Aysén fjords (44-46°S). These master faults dips towards each other at a right step-over, connected by secondary NE-striking faults, thus suggesting a palm-three geometry (Thomson, 2002; Woodcock & Fischer, 1986). The present-day activity of the LOFS was well-established during the Aysén seismic swarm in 2007 (Lange et al., 2008; Legrand et al., 2011). This swarm occurred beneath the duplex area, ending in two large events of magnitudes $M_w = 6.1$ and $M_w = 6.2$, of extensional and strike-slip kinematics, respectively. It is argued that these swarm was both volcanic and tectonically driven, whereas the culminating event of $M_w = 6.2$ was generated for the local change in Coulomb stress caused by the previous extensional event (Russo et al., 2011). Whereas these events occurred in a brittle regime of the crust, the stress and kinematic regimes in the brittle-plastic transition beneath are still poorly understood.

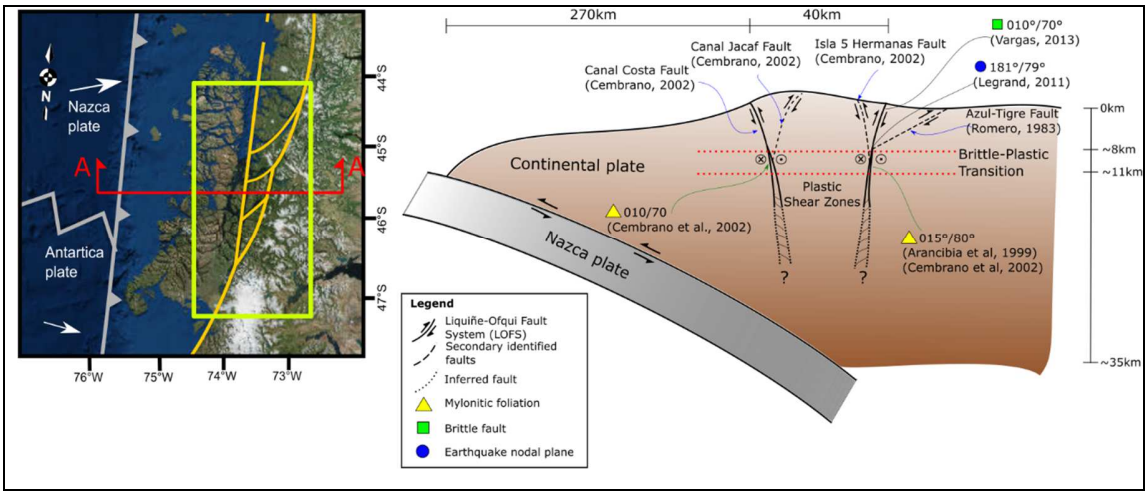

Figure 1-17: (*left*) The continental margin at 44-47S° latitude, showing the location of the LOFS duplex.in the green square. (*right*) A schematic vertical section of the continental lithosphere in

orientation A-A. Geological and seismic data is projected on a representative LOFS section, which displays the orientation (ρ/μ) of brittle and brittle-plastic fault planes.

1.3 Statement of the problem

The state of stress at plate boundary intra-arc fault systems and the interaction between crustal deformation and magmatism has been an important topic of research for decades (e.g. Beck, 1983; Blanquat & Tikoff, 1998; McCaffrey, 1992; Pérez-Flores et al., 2016). Faults responds both to tectonic stress and magma overpressure, whereas magma requires local extension for upward migration. This involves a complex mechanical feedback, where faults spatial distribution and the crust rheology play an important role. In the past decades, unravelling this interaction has been mostly constrained in the brittle portion of the lithosphere. However, the mechanisms, stress regimes and kinematics in the stronger brittle-plastic domain are still undergoing through debate. It is agreed, nevertheless, that local transient extension must exist, at least down to the intrinsic length of plasticity, for magma to migrate through the lithosphere.

Furthermore, fault systems are often arranged in a complex distribution of segments, whose interaction is not only related to fluid transport, but to the seismic hazard these faults presents by themselves. Strike-slip duplexes are structures that are commonly developed within transcurrent fault systems, as in the case of the LOFS in the Southern Andes. It is of general interest how these different fault segments respond to the local kinematics of their adjacent counterparts and the overall tectonic regime. Understanding their mechanical behavior, stress state and tectonic-magmatic interaction, is not only important for a fundamental tectonics study, but also to seismic and volcanic hazard assessment and geothermal potential.

A well constrained case study is the LOFS Aysén seismic swarm, where the connection between the fault system kinematics, its seismicity and magma migration was established (Legrand et al., 2011). The initial mechanical conditions upon which this swarm was

generated can provide insights of how and where volcanism takes place within a fault system. In this context, numerical simulations can simulate the tectonic and mechanical behavior of a fault system, thus improving our knowledge of how volcanic arcs mechanically behave.

1.4 Objectives

In this work, we study the steady-state stress field acting on the LOFS current geometry, by means of mechanical modeling and numerical simulations, identifying key aspects such as the fault system kinematics and stress regimes that enhance (or prevent) magma transport through the lithosphere. Furthermore, we calculate the velocity field within the continental lithosphere to analyze the LOFS duplex heterogeneous distribution of slip rates and stress regimes, and how they are related to slip partitioning of the South-Andes margin and its orogenic process.

To accomplish these objectives, we incorporate the tectonic boundary conditions, crust rheology and the LOFS geometry to a numerical model, which is resolved through the Finite Element Method (FEM) to calculate the elastic-plastic response of the fault system.

1.5 Hypothesis

The main hypothesis of this work is that both master faults of the LOFS undergo different states of stress, with the eastern master fault likely accommodating most of the margin-parallel component of the convergence vector, whereas the western master fault takes up the compressional margin-orthogonal component, thus enabling the main cordillera to differentially uplift with respect to the forearc and backarc regions.

Further, I speculate that secondary faults of the LOFS act as long-lived conduits for magma to vertically migrate, due to the extensional stress regime with which they are loaded, especially where they are close to the intersection with a master fault.

Finally, I hypothesize that the spatial distribution of the LOFS allows a positive or negative feedback between its segments kinematics and stress regimes. Close to a fault intersection, fault segments where the tectonic loading superimposes on the adjacent fault local kinematics will have their slip rates enhanced, in contrast to segments where both factors acts in an opposite sense.

1.6 Methodology

To solve the displacement $\boldsymbol{u}(\boldsymbol{x})$, strain $\boldsymbol{\varepsilon}(\boldsymbol{x})$ and stress $\boldsymbol{\sigma}(\boldsymbol{x})$ fields over the continental margin, a continuum-mechanical model is postulated, which addresses the spatial distribution and rheology of the rocks composing the LOFS and the continental lithosphere. This continuum model, as its name states, assumes rock bodies and faults as continuum solids rather than discrete elements. Both the linear and angular balance equations, as well as the rheology relations are described by a set of partial differential equations, which are solved in space by the Finite Element Method (FEM).

1.6.1 Continuum governing equations in elasto-plasticity

To model the steady-state long-term behavior of the continental margin, we neglect the inertial terms of the linear-momentum balance principle. Thus, within a Lagrangian framework of movement description, the equilibrium equation is reduced to:

$$\nabla \cdot \boldsymbol{\sigma} + \rho \boldsymbol{g} = \boldsymbol{0} \qquad \textbf{Equation 1-9}$$

Where $\nabla \cdot ()$ is the divergence operator, ρ the rock's density and $\boldsymbol{g}$ is the gravity vector field. This equation describes the equilibrium of an infinitesimal body. Let $\boldsymbol{u}(\boldsymbol{x})$ be the displacement field of each point in the continental lithosphere. Then, we define the infinitesimal strain tensor as $\boldsymbol{\varepsilon}(\boldsymbol{x}) = \frac{1}{2}(\nabla \boldsymbol{u} + \nabla \boldsymbol{u}^{\boldsymbol{t}})$. Assuming an elasto-plastic behavior, an additive decomposition of strain assumed, which takes the form:

$$\boldsymbol{\varepsilon} = \boldsymbol{\varepsilon}^{e} + \boldsymbol{\varepsilon}^{p} \qquad \textbf{Equation 1-10}$$

where $\boldsymbol{\varepsilon^{e}}$ is the elastic strain component, and $\boldsymbol{\varepsilon}^{p}$ plastic strain component. The associated stress in the solid with elastic rheology will be described in terms of Hooke's law using the fourth-order elasticity tensor $\boldsymbol{C}$ and the strain tensor:

$$\boldsymbol{\sigma}(\boldsymbol{x}) = \boldsymbol{C} : \boldsymbol{\varepsilon^{e}} \qquad \textbf{Equation 1-11}$$

where : is the tensor contraction operator. In the following, it will be useful to define the effective plastic strain $\underline{\varepsilon}^{p}$ and the effective deviatoric stress $\underline{\sigma}$.

$$\underline{\boldsymbol{\varepsilon}}^{\boldsymbol{p}} = \sqrt{\frac{2}{3}\boldsymbol{\varepsilon}^{p} : \boldsymbol{\varepsilon}^{p}} \qquad \textbf{Equation 1-12}$$

Defining the deviatoric stress tensor $\boldsymbol{s} = \boldsymbol{\sigma} - \boldsymbol{pI}$ in terms of the mean pressure $\boldsymbol{p}$, we build the effective deviatoric stress

$$\underline{\sigma} = \sqrt{\frac{1}{2}\boldsymbol{s} : \boldsymbol{s}} \qquad \textbf{Equation 1-13}$$

Within the framework of rate-independent, associated flow-plasticity we can describe the plastic behavior of a material by a yield function $\boldsymbol{\varphi}(\boldsymbol{\sigma}, \boldsymbol{\varepsilon})$, a flow rule $\dot{\boldsymbol{\varepsilon}}^{\boldsymbol{p}}(\boldsymbol{\delta\varphi}/\boldsymbol{\delta\sigma})$ and a hardening law $\boldsymbol{\tau_{crit}}(\boldsymbol{\varepsilon^{p}})$. To represent the brittle-plastic transition, an isotropic von-Mises yield function is suggested in Section 1.1.2:

$$\varphi(\boldsymbol{\sigma}, \boldsymbol{\varepsilon}) = \underline{\sigma} - \tau_{y}\left(\underline{\varepsilon}^{p}\right) \leq 0 \qquad \textbf{Equation 1-14}$$

When the yield function is $\varphi < 0$ the material behaves elastically and plastically when $\varphi > 0$. In flow plasticity, the yield function will never be greater than 0, but rather grow accordingly to the hardening law, for which we select an exponential hardening law in its saturation form:

$$\tau_{crit}\left(\underline{\varepsilon}^{p}\right) = \tau_{\infty} + (\tau_{0} - \tau_{\infty})e^{-\beta\underline{\varepsilon}^{p}} \qquad \textbf{Equation 1-15}$$

The value τ_∞ represents the saturation strength of the rock at high levels of deformation, whereas τ_0 represents the initial strength while it has never behaved plastically before. The hardening exponential rate β, represents at which rate of $\underline{\varepsilon}^p$ the strength changes from the initial to the saturation value by representing an asymptotic curve. This is typically the plastic behavior of rocks in general under plastic behavior, particularly for mylonites. This characterization of a rock's rheology is commonly used to homogenize a rock mass, with several randomly-oriented fractures, thus describing an effective stress-strain relationship.

1.6.2 Continuum model and boundary conditions

To solve the displacement and stress in the LOFS, a computational model is constructed (Figure 1-18), which represents the continental margin at the latitude of the Aysén duplex. It represents a 1km-width horizontal slice of the lithosphere at the depth of the brittle-plastic transition in the LOFS (10 km-depth). The model has a dimension of 400km E-W from the subduction trench eastward and 400km N-S with the LOFS duplex at the center.

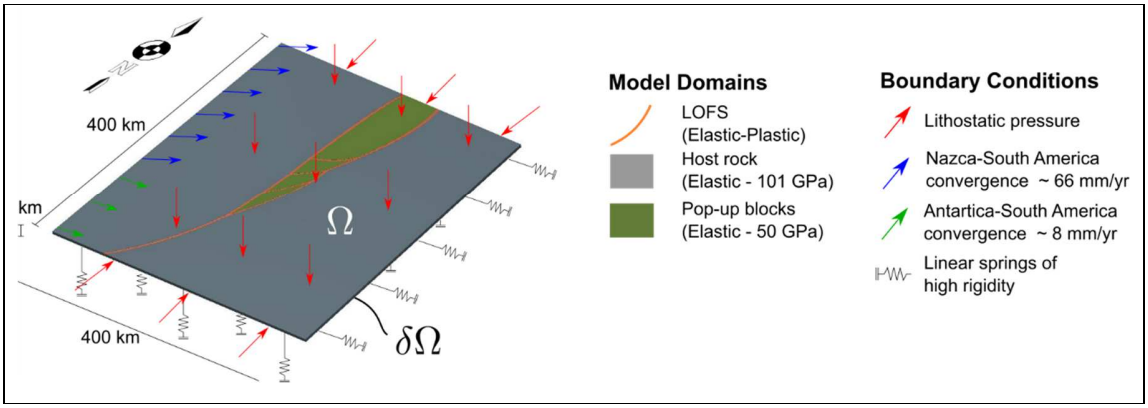

Figure 1-18: The continuum model representing the continental lithosphere (Ω) including the LOFS geometry. The model domains represent the host rock and pop-up blocks, which have an elastic constitutive relation, whereas the LOFS is represented through a elasto-plastic behavior. Boundary conditions are set through the domain boundary ($\delta\Omega$), where the convergence between Nazca,

Antarctica and South-American plates are set as Dirichlet boundary conditions ($\boldsymbol{u(\delta\Omega) = a_0}$) and lithostatic pressure, buoyancy and the weight of the South-America plate westward of the model are set as Newmann boundary conditions ($\boldsymbol{\partial u/\delta x(\delta\Omega) = b_0}$).

The model differentiates between the host rock and the LOFS. The first is depicted through a linear-elastic rheology, with constant values of Elastic modulus (E) and poisson ratio (ν). Using P-wave velocities from seismic inversions (Barrientos et al., 2004) and density values from gravity surveys (Introcaso et al., 1992), which represents the typical values of the South-Andean margin, we obtain the elastic modulus of the forearc

$$E = \rho V_p^2 \frac{(1+\nu)(1-2\nu)}{(1-\nu)} \qquad \textbf{Equation 1-16}$$

The latter is set to 101GPa, considering the upper bound obtained. A value of $\nu = 0.25$ is used to represent a typical granitic host rock. Pop-up blocks are distinguished from the forearc and backarc by decreasing its Elastic modulus to 50GPa, as an attempt to represent its more fractured state due to recurrent/previous faulting, while still behaving elastically at a macroscopic scale. This assumption is supported by the fact that the crustal thermal gradient is increased in its location, thus diminishing its value of E. The LOFS is modeled by an elastic-plastic constitutive relation, using an isotropic von-Mises yield criteria with associated flow rule and isotropic hardening. Values of τ_0 and τ_∞ are set to 20MPa and 8MPa respectively, to represent the range of experimentally deformed mylonites (White et al., 1980). The hardening exponential rate β is set to 100, intended to modulate the quick asymptotic behavior of τ_y between the ranges of $\underline{\varepsilon}^p = 0$ and 0.05.

The convergence between Nazca and South-America plate (66mm/yr) (DeMets et al., 2010) is simulated through a velocity (displacement at each Δt) boundary condition (Dirichlet type), along with the Antarctica-South-America convergence (8mm/yr). The roughly null relative velocity west of the model, due to the entire weight of the South-America plate westward, is simulated through linear-elastic springs of high rigidity. The

buoyancy of the entire lithosphere downward is also simulated by the use of these springs. The overburden pressure is represented through surface loading on top of the model and N-S boundaries.

1.6.3 The finite element method for elasto-plastic solids

The set of partial differential equations (PDE) defined in 1-9, 1-10, 1-11, 1-15 and 1-16, in conjunction with the domain boundary conditions, represent an Initial Boundary Value Problem (IBVP) in its strong formulation, whose solution is approximately solved by the finite element method (FEM). Here we summarize the main steps for the development of an elasto-plastic FEM. A detailed review of the Finite Element Method can be found in Zienkiewicz & Taylor, (2000), whereas specialized FEM in elasto-plasticity algorithms can be found in Neto et al., (2011)

First, an equivalent equilibrium statement must be provided in a weak version, which relaxes the smoothness condition on the first derivative of $\boldsymbol{u}$. Through integration by parts, Equation 1-9 is directly integrated and rewritten as:

$$\int_{\Omega} \{\boldsymbol{\sigma}(\nabla \boldsymbol{u}) : \nabla \boldsymbol{v} - \rho \boldsymbol{g} \cdot \boldsymbol{v}\} dV - \int_{\delta\Omega} \boldsymbol{v} \cdot \boldsymbol{\sigma}(\nabla \boldsymbol{u}) \boldsymbol{n}\, dS = 0 \quad \forall \boldsymbol{v} \in \boldsymbol{\mathcal{V}} \qquad \textbf{Equation 1-17}$$

Here, $\boldsymbol{v} \in \boldsymbol{\mathcal{V}}$ is a test function that belongs to the space of virtual displacements $\boldsymbol{\mathcal{V}}$ or kinematically admissibly solutions and $\boldsymbol{\sigma}(\boldsymbol{\nabla u})$ is the stress tensor calculated from the solution $\boldsymbol{u}$, which is unknown a priori. Given that Equation 1-17 holds true for any $\boldsymbol{v}$, the solution $\boldsymbol{u}$ can be retrieved using a numerical integration. In particular, we use a spatial discretization base on the finite element method.

To this end, we construct an approximate solution $\boldsymbol{u}^h(\boldsymbol{x})$ to the domain's displacement field for a given set of boundary conditions and material behavior, by discretizing the

domain into several nodes and elements connecting them. To integrate the presented weak formulation at each element, their approximated displacement field $\tilde{\boldsymbol{u}}^e(\boldsymbol{x})$ is interpolated in terms of the element's nodal displacement ($\boldsymbol{u}_a^e$) through shape functions $N_a^e(\boldsymbol{x})$ of each node a.

$$\tilde{\boldsymbol{u}}^e(\boldsymbol{x}) = \sum_{i=1}^{n_{node}} N_a^e(\boldsymbol{x})\boldsymbol{u}_a^e = \mathbf{N^e u}^e \qquad \textbf{Equation 1-18}$$

$$\nabla\tilde{\boldsymbol{u}}^e(\boldsymbol{x}) = \sum_{i=1}^{n_{node}} \frac{\partial N_a^e(\boldsymbol{x})}{\partial \boldsymbol{x}}\,\boldsymbol{u}_a^e = \mathbf{B^e u}^e \qquad \textbf{Equation 1-19}$$

Here, matrices **N** and **B** are defined for computational purposes and mathematically loosely defined, given that its implementation depends on the dimensionality and type of elements used in the discretization. It is worth mentioning that $\boldsymbol{v}$ can also be discretized using Equation 1-18. Thus, considering that Equation 1-17 holds true for any $\boldsymbol{v}$, Equation 1-17 can be rewritten for each element as:

$$\left\{\int_{\Omega^e}\{(\mathbf{B}^e)^t\boldsymbol{\sigma} - (\mathbf{N}^e)^t\,\rho\boldsymbol{g}\}dV - \int_{\delta\Omega^e}(\mathbf{N}^e)^t\boldsymbol{\sigma}\boldsymbol{n}\,dS\right\}\boldsymbol{v} = 0 \quad \forall\boldsymbol{v}\in\boldsymbol{\mathcal{V}} \qquad \textbf{Equation 1-20}$$

Thus, the left side of Equation 1-20 in brackets should vanish. Finally, the weak formulation is stated the equilibrium between internal and external forces acting over the domain at hand:

$$\mathbf{f}_{\text{int}} - \mathbf{f}_{\text{ext}} = \mathbf{0}$$

$$\bigwedge_{e=1}^{n_{elem}} \mathbf{f}_{\text{int}}^e - \bigwedge_{e=1}^{n_{elem}} \mathbf{f}_{\text{ext}}^e = \mathbf{0} \qquad \textbf{Equation 1-21}$$

$$\bigwedge_{e=1}^{n_{elem}} \int_{\Omega}(\mathbf{B}^e)^t\boldsymbol{\sigma}\,dV - \bigwedge_{e=1}^{n_{elem}}\left\{\int_{\Omega}(\mathbf{N}^e)^t\,\rho\boldsymbol{g}\,dV + \int_{\delta\Omega}(\mathbf{N}^e)^t\boldsymbol{\sigma}\boldsymbol{n}\,dS\right\} = \mathbf{0}$$

In here, $\bigwedge$ represents the assembly of the element's internal/external forces throughout the entire discretized domain. Thus, the internal and external forces are assembled computationally considering each element at equilibrium. However, for path-dependent materials, such as in elasto-plasticity, Equation 1-21 does not hold truth straight forward, but rather an iterative scheme is necessary.

Let $\boldsymbol{\sigma}_{n+1} = \hat{\boldsymbol{\sigma}}(\underline{\varepsilon}_n^p, \boldsymbol{\varepsilon}_{n+1})$ be the stress in step $n+1$, which is defined according to an incremental constitutive function. The outcome of this procedure is expected to converge to an exact solution as the strain increments are reduced. Furthermore, the global equilibrium as defined in Equation 1-21, can be defined as:

$$\boldsymbol{r}(\boldsymbol{u}_{n+1}) = \mathbf{f}_{\text{int}}(\boldsymbol{u}_{n+1}) - \mathbf{f}_{\text{ext}}(\boldsymbol{u}_{n+1}) \rightarrow \mathbf{0} \qquad \textbf{Equation 1-22}$$

In here, convergence is defined when for a given $\boldsymbol{u}_{n+1}$ the value of $\frac{\boldsymbol{r}^{\boldsymbol{m+1}}}{\mathbf{f}_{\text{ext}}{}^{m}} < \epsilon_{tol}$ holds true within a step m for an equilibrium convergence tolerance ϵ_{tol}, which is commonly achieved through a Newton-Raphson scheme.

2. STATES OF STRESS AND SLIP PARTITIONING IN A CONTINENTAL SCALE STRIKE-SLIP DUPLEX: TECTONIC AND MAGMATIC IMPLICATIONS BY MEANS OF FINITE ELEMENT MODELING. (Article published in *Earth and Planetary Science Letters*)

2.1 Introduction

Regional crustal stress in convergent margins is commonly compartmentalized as faults with various orientations within the continental lithosphere. Faults locally disrupt the stress field, where the variation of stress orientations and relative magnitudes lead to different mechanisms of seismic faulting and fluid migration (e.g. Nakamura et al., 1977; Rubin, 1995; Sibson, 1994), which uses conduits located in not only brittle, but also ductile shear zones (e.g. Hutton, 1988). Furthermore, brittle faulting occurs near the surface, typically under the Mohr–Coulomb criterion, whereas thermo-activated crystal–plastic deformation mechanisms take place as depth and temperature increases (McClay, 1977; Tullis & Yund, 1987). These mechanisms include, but are not limited to, dislocation creep (climb and glide) beneath the brittle-plastic transition and diffusion creep (e.g. Cobble and Nabarro- Herring creep, both sensitive to grain-size) in deeper structural levels. However, the precise relationship between magma transport and deformation mechanisms in plastic shear zones (i.e. beneath the seismogenic region) remains speculative. It is established that a strong dependence on viscosity contrast between host rock and magma composition should be taken into account of such relationship (Rubin, 1993). While seismic pumping is capable to transporting large volumes of magma, crystal–plastic mechanisms in mylonites develop large, low-permeability crack networks that could serve as magma transport conduits (e.g. Bauer et al., 2000). Therefore, regardless of the transport mechanism, local extension must exist (at least down to the intrinsic length scale of plasticity) for magma to migrate, thus ensuring kinematic compatibility.

In this context, transcurrent fault systems are large-scale shear zones that cut through the lithosphere, generally driven by oblique plate convergence. They are composed of a series of anastomosed faults striking sub-parallel to the plate margin, thus accommodating a significant part of the convergence margin-parallel component (Teyssier et al., 1995). Also, they are commonly arranged in two or more conjugate sets of opposite-verging faults (e.g. Braun & Beaumont, 1995), which could be connected by second-order structures: such is the case of strike-slip duplexes (Woodcock & Fischer, 1986).

An outstanding case study of a regional-scale transcurrent shear zone, is the Liquiñe–Ofqui Fault System (LOFS) (Figure 2-1), which is located within the South-Andean margin. It runs over 1100 km from south of the Ofqui isthmus (48◦S) to Alto Bio-bio (37 ◦S) (e.g Melnick et al., 2006). The LOFS is described as a long lived intra-arc structure that has been active – at least – since 6 Ma (Cembrano et al., 2002). Geological evidence (e.g. Arancibia et al., 1999; Lavenu & Cembrano, 1999), along with seismic (Lange et al., 2008) and geodetic observations (Wang et al., 2007) documents its overall transpressional dextral kinematics.

The LOFS deformation is genetically associated and kinematically consistent with: (i) NNE and NE alignments of volcanic centers (Cembrano & Lara, 2009; Nakamura et al., 1977); (ii) sharp geomorphic lineaments, where faulting contributed to the land-scape evolution by differential erosion since the Pliocene (Cembrano et al., 1996; Glasser & Ghiglione, 2009); (iii) high denudation rates (1 mm/yr) due to the balance between transpressional surface uplift and high glacial erosion rates (Thomson, 2002); (iv) shallow seismicity (<10 km) (Cembrano & Lara, 2009; Lange et al., 2008; Legrand et al., 2011); and (v) active hydrothermal reservoirs and fault-vein networks associated with paleofluid flow (e.g. Sánchez et al., 2013). Hence, the importance of studying LOFS deformation goes from fundamental tectonics to hazard assessment and geothermal potential.

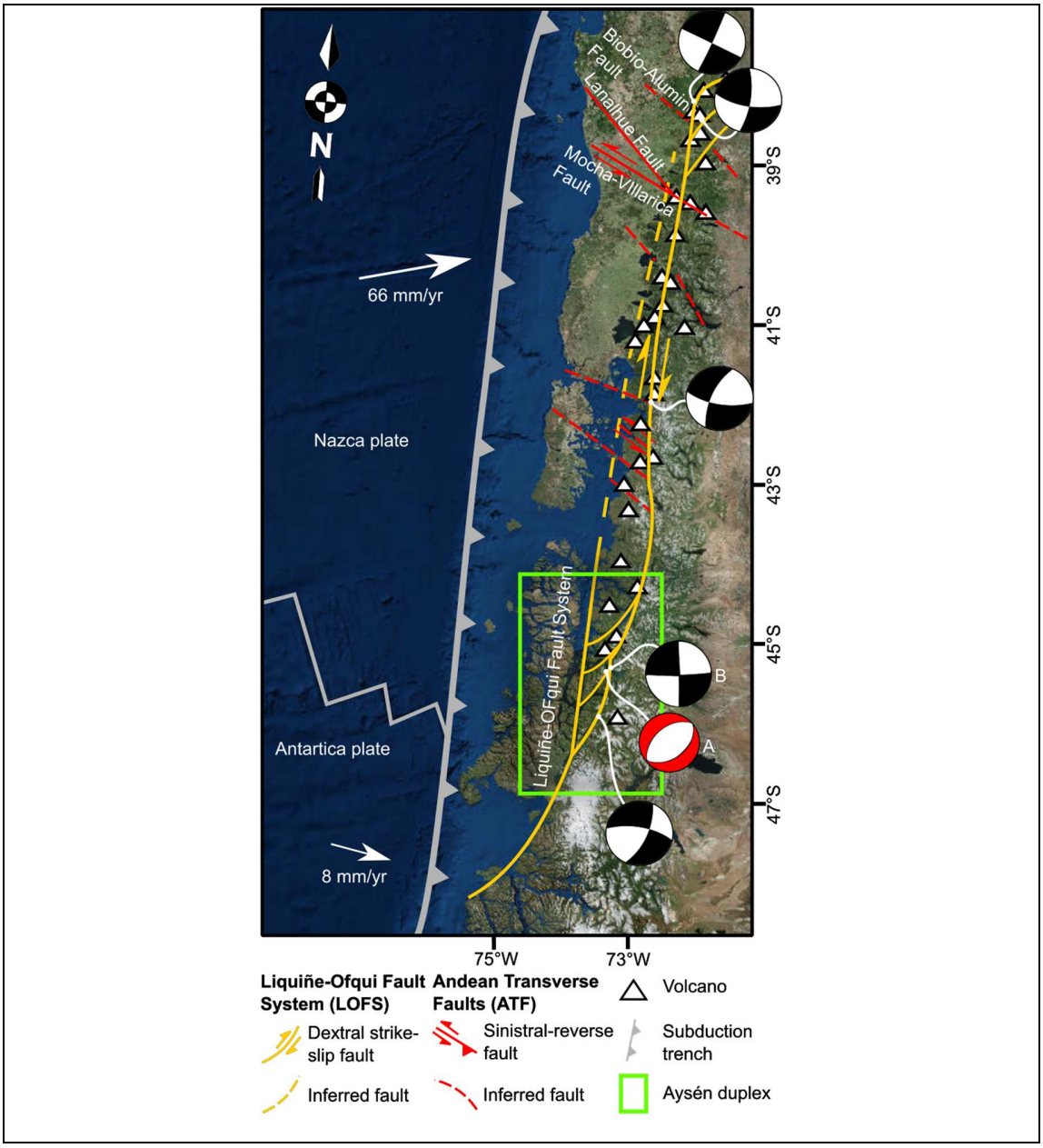

Figure 2-1: Tectonic setting showing the main strands of the LOFS within the South- Andean margin. Andean Transverse Faults [ATF] are shown in red (modified from Sánchez et al., 2013), along with representative stratovolcanoes of the volcanic arc. The southern Aysén duplex is highlighted in the green frame. Main historical focal mechanisms of the LOFS are shown (Lange et al., 2008) along with

the Aysén swarm culminating events (A represents the 3/02/2007 *Mw* = 6.1 extensional earthquake and B the 3/21/2007 *Mw* = 6.2 strike-slip earthquake) (Legrand et al., 2011).

The LOFS present-day interplay between tectonics and magma transport was clearly documented during the Aysén duplex seismic swarm in 2007 (Lange et al., 2008; Legrand et al., 2011). Thousands of earthquakes occurred within the duplex domain, ending in two large events of magnitudes *Mw* = 6.1 and *Mw* = 6.2, see Figure 2-1. The first event was both volcanic and tectonically driven with normal-extensional focal mechanism, most likely caused by dike upward propagation. This event subsequently activated a LOFS master fault in a second seismic event, displaying a well-constrained strike-slip focal mechanism. However, the stress state and kinematic regimes at the brittle–plastic transition, right beneath where the seismic swarm was nucleated (8–10 km), are still poorly understood.

In this work, we examine the stress and deformation fields at the LOFS strike-slip duplex within the brittle–plastic transition using numerical simulations. Our main goal is to understand the interaction between adjacent fault segments of a strike-slip duplex and suitable tectonic settings for magma upward migration; particularly, we estimate the steady-state stress-field acting on the LOFS current geometry, and use it as a basis for detecting favorable fluid transport conditions. Further, we calculate the velocity field within the continental lithosphere and slip rates of the LOFS duplex segments, to answer open questions such as: How is slip partitioned along and across the continental margin and why? What are the LOFS slip rates and their distribution along strike? To this end, we develop a finite element model (FEM) of the LOFS duplex that reproduces a horizontal slice of the continental lithosphere at and beneath the brittle–plastic transition. Using a continuum-mechanics formulation that considers elastoplastic material behavior, we model the LOFS duplex geometry (i.e. structures are represented as volumes rather than discontinuities) and the surrounding wallrock. To validate our numerical model, we confront our results with seismic and geological data recorded in the field.

2.2 Geotectonic framework

The tectonics of the Andes Southern Volcanic Zone is controlled by convergence and subduction between the Nazca and South- American plates. The Peru–Chile trench trends N10◦E, whereas the convergence velocity vector trends N80◦E at 66 mm/yr (Angermann et al., 1999) (Figure 2-1). This obliquity angle (≈ 20◦ counter-clockwise) has remained roughly the same for the last 10 Ma (Argus et al., 2010; Kendrick et al., 2003) and is sufficient for slip partitioning to partially occur within the Southern Andes intra-arc (Arancibia et al., 1999; Lavenu & Cembrano, 1999; Stanton-Yonge, 2016). However, south of the Chilean Triple Junction (between Nazca, South-America and Antarctica plates at 46◦ latitude), convergence between Antarctica and South America is mainly orthogonal to the trench (DeMets et al., 2010).

Several oblique-to-the-arc faults are found along the LOFS (Cembrano & Lara, 2009). They consist either of secondary structures splaying off the LOFS or ancient basement inherited faults (e.g. Stanton-Yonge et al., 2016, and references therein). The latter have been grouped into the so-called Andean Transverse Faults [ATF] (shown in red in Figure 2-1). Most of them are cut and/or dis-placed by the LOFS master faults. In the northern end of the LOFS, a horse-tail structure is displayed (Melnick et al., 2006; Pérez-Flores et al., 2016), whereas in the south, two large NNE-trending master faults form a strike-slip duplex at a right step-over (Cembrano et al., 1996) (Figure 2-1). The latter is located within the Aysén fjord (44–46◦S), where quartz-feldspathic mylonitic rocks and upper crustal faults have been exhumed from depths of a few kilometers. Both document compressional to transpressional deformation events (Arancibia et al., 1999; Lavenu and Cembrano, 1999; Vargas et al., 2013).

The LOFS duplex runs mostly through the North Patagonian batholith, consisting of Late Cenozoic granitoids, which intrude Paleozoic metamorphic complexes (Hervé, 1993) and

Early Cenozoic volcano-sedimentary rocks. Within the LOFS domain, plastic deformation localizes in discrete anastomosed mylonitic rock bands, with widths ranging from 1 cm to 1 m. They are distributed within large encompassing fault zones, whose total width may reach up to 4 km (Cembrano et al., 1996). The duplex consists of two master faults that dip towards each other at a right step-over, thus suggesting a palm-tree geometry (Thomson, 2002). Similar steep dips documented on brittle-faults and mylonitic bands (Arancibia et al., 1999;Cembrano et al., 2002; Vargas et al., 2013) suggest the continuity of this geometry, at least down to the brittle–plastic transition (Figure 2-2). However, the distance between both master faults at the surface (≈ 40 km), along with their steep dips, implies that the master faults should not coalesce at the brittle–plastic transition (8–11 km depth), in opposition to what was suggested by Thomson, (2002). Therefore, constraints set by the duplex geometry at the surface, the observed fault dip and crustal seismicity could only be attainable if the coalescing point were well underneath the brittle–plastic transition. One significant, independent evidence for the LOFS master faults depth is provided by a series of monogenetic volcanic cones built on top of surface fault traces (Lara et al., 2008). The mantelic geochemical signature of the magmas suggests they were transported at a geologically instantaneous rate along sub-vertical paths from the underlying asthenosphere (Cembrano and Lara, 2009). Moreover, numerical simulations of strain partitioning across transpressional plate boundaries in transcurrent shear zones (Braun & Beaumont, 1995) suggest such master faults should coalesce close to the asthenospheric wedge

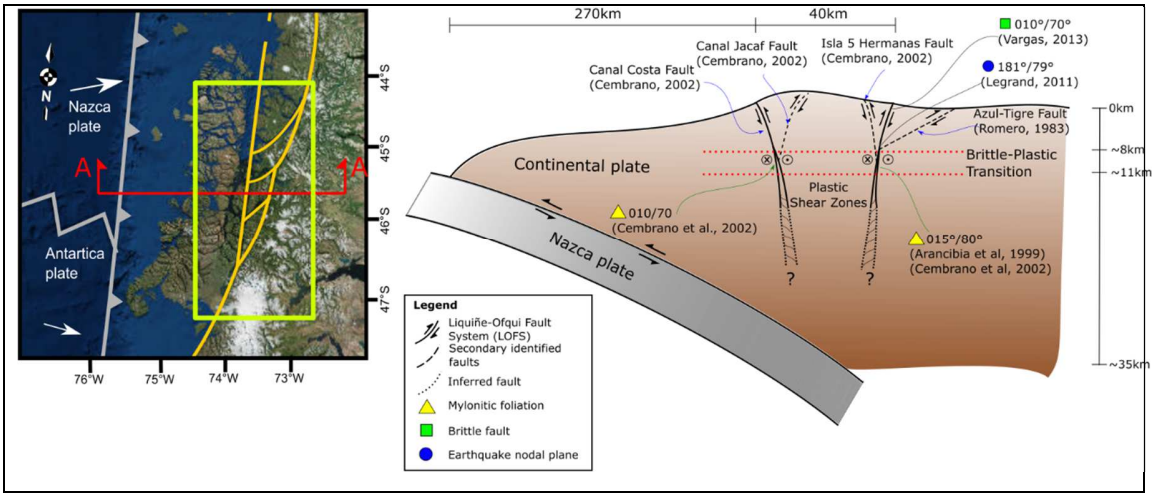

Figure 2-2: Schematic vertical section of the continental lithosphere in orientation A–A. Previous work data and field mapping are projected in a representative LOFS section.

2.3 Methodology

. To address the mechanics of the LOFS, we consider an elasto-plastic continuum formulation, which is solved using a finite-element numerical scheme, as is detailed next.

2.3.1 Continuum governing equations

We consider the crust and LOFS domain as a continuum solid, which must satisfy the linear-momentum balance principle. Assuming a quasi-static problem, we neglect inertial terms, and the balance equations reduce to the differential equilibrium equation

$$\nabla \cdot \boldsymbol{\sigma} + \rho \boldsymbol{g} = \mathbf{0} \qquad \textbf{Equation 2-1}$$

where bold fonts are used to represent vectors and tensors and normal fonts to represent scalars, $\boldsymbol{\sigma}$ is the Cauchy stress tensor, $\nabla \cdot ()$ represents the divergence operator, ρ is the rock density, and $\boldsymbol{g}$ is the gravity vector field. Let $\boldsymbol{u}(\boldsymbol{x})$ be the displacement field, then

the strain tensor is $\boldsymbol{\varepsilon} = 1/2(\nabla \boldsymbol{u} + \nabla \boldsymbol{u}^t)$, where $\nabla(\cdot)$ is the gradient operator. To account for elastic–plastic behavior, we decompose the strain tensor into its elastic strain and plastic strain components, represented by $\boldsymbol{\varepsilon}^e$ and $\boldsymbol{\varepsilon}^p$, respectively, and write:

$$\boldsymbol{\varepsilon} = \boldsymbol{\varepsilon}^e + \boldsymbol{\varepsilon}^p \qquad \textbf{Equation 2-2}$$

Then, the stress is defined in terms of the elastic strain:

$$\boldsymbol{\sigma} = \boldsymbol{C} : \boldsymbol{\varepsilon}^e \qquad \textbf{Equation 2-3}$$

where the operator : denotes a tensor contraction and $\boldsymbol{C}$ is the fourth-order elasticity tensor, assumed to be isotropic. It is useful to refer to the plastic behavior by defining the effective plastic strain

$$\underline{\varepsilon}^p = \sqrt{\frac{2}{3}\boldsymbol{\varepsilon}^p : \boldsymbol{\varepsilon}^p} \qquad \textbf{Equation 2-4}$$

Throughout this work, which addresses the mechanical state in the brittle–plastic transition, we consider a yield criterion and flow law dependent of plastic strain ($\underline{\varepsilon}^p$) and pressure-independent (p). The implications of this particular choice will be further discussed in Section 2.5.1. We define the deviatoric stress tensor by $\boldsymbol{s} = \boldsymbol{\sigma} - \boldsymbol{pI}$ and the effective deviatoric stress as:

$$\underline{\sigma} = \sqrt{\frac{1}{2}\boldsymbol{s} : \boldsymbol{s}} \qquad \textbf{Equation 2-5}$$

Plastic behavior onset in the solid media is determined by the yield function $\varphi(\boldsymbol{\sigma}, \underline{\varepsilon}^p)$, which for a von-Mises yield criterion takes the form

$$\varphi(\boldsymbol{\sigma}, \boldsymbol{\varepsilon}^p) = \underline{\sigma} - \tau_y\left(\underline{\varepsilon}^p\right) \leq 0 \qquad \textbf{Equation 2-6}$$

where τy represents the critical shear strength, which evolves according to the exponential hardening law (Voce, 1955).

$$\tau_y\left(\underline{\varepsilon}^p\right) = \tau_\infty + (\tau_0 - \tau_\infty)\exp(-\beta\underline{\varepsilon}^p) \qquad \textbf{Equation 2-7}$$

Here, τ_0 represents the initial shear strength, and τ_∞ the saturation shear strength, whereas β is a hardening exponential rate. Although this is a general approximation, it is commonly used to describe the strain-hardening stage of geomaterials, through the homogenization of a fractured rock mass (e.g. Pouya & Ghoreychi, 2001). Summarizing, Equations 2-1, 2-2, 2-3, 2-6 and 2-7 represent a set of partial differential equations, which along boundary conditions for the displacements and tractions constitute an initial boundary value problem.

2.3.2 Finite element model

To numerically solve the governing initial boundary value problem, we propose to use the finite element method for an elastic– plastic material formulation (Neto et al., 2011), where a Lagrangian framework is assumed. For a complete treatment of finite element formulations in solid mechanics the reader is referred to Zienkiewicz & Taylor, (2000). As a first step, a 3D discretization of the domain was generated to obtain a tetrahedral mesh. It represents a horizontal 1 km-thick slice of the continental lithosphere, in which we included the LOFS geometry at the brittle–plastic transition. Two different setups were considered: one at 10 km depth and the other at 15 km. Figure 2-3 shows the model representation of the continental lithosphere encompassing the LOFS duplex 400 km east of the trench, with a 400 km length along the NS axis. Dimensions of the model were extended away of the strike-slip duplex, to minimize the influence of boundary conditions on the distribution of deformation in and around the fault duplex. The model was built by first meshing the domain with coarse elements. The mesh was adaptively refined towards the fault system, where a finer mesh is required to better reflect the geometry and increase the numerical accuracy of the FE solution. The mesh-generation process was performed

using ANSYS Meshing 15.0, creating a total of $1.3 \cdot 10^6$ elements with a mean and maximum of 1.14 and 3.96 radius ratio, respectively.

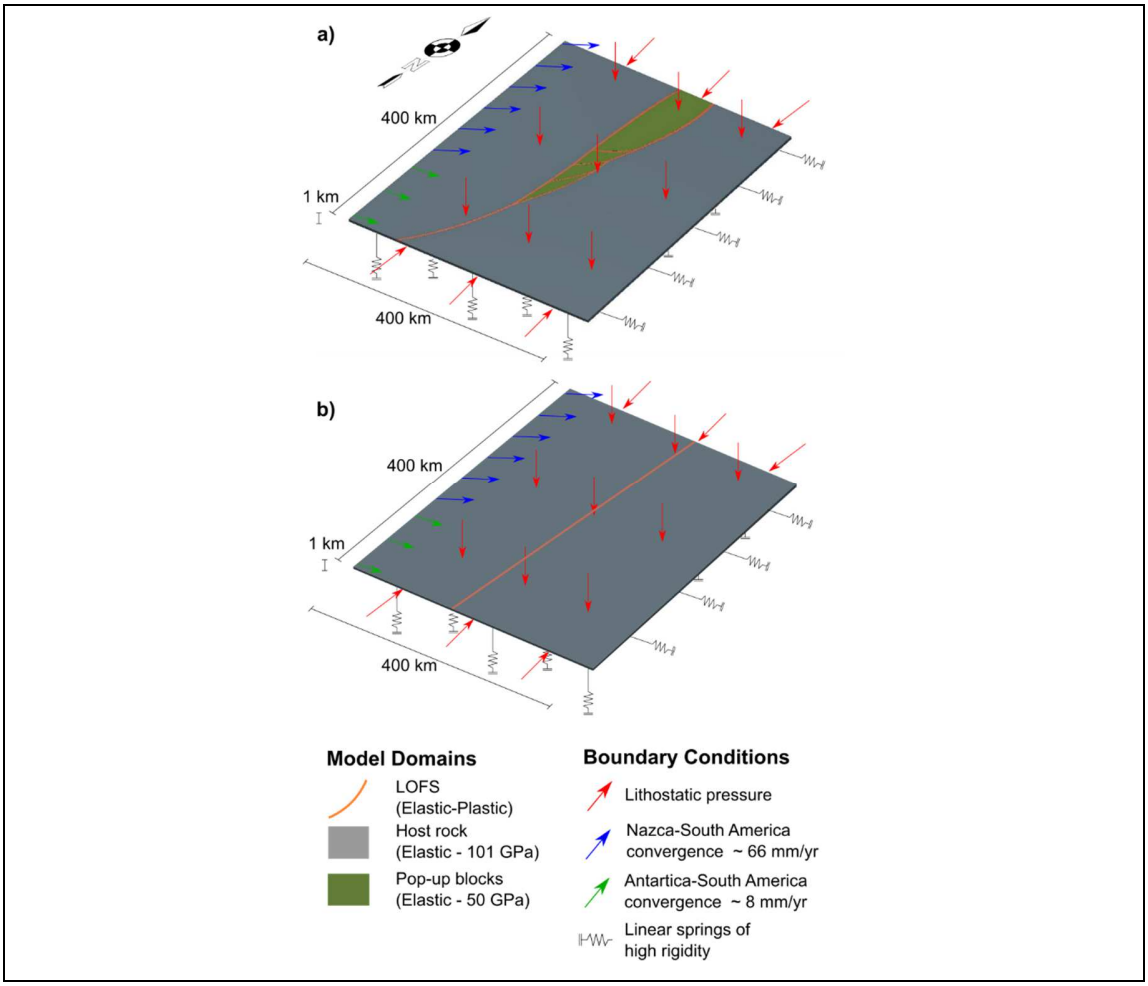

Figure 2-3: Domains spatial distribution and boundary conditions used in the models. Model (a) represents the LOFS at 10 and 15 km depth and its boundary conditions. Model (b) is an equivalent single-fault model, using the same material properties and boundary conditions than model (a).

Three regions with different material properties were considered within the model domain: host rock, pop-up blocks and fault zone rocks; see Figure 2-3. The elastic modulus E and Poisson's ratio ν of the host rock were set to 101 GPa and 0.25

respectively, calculated using a density of $\rho = 2800 \frac{\text{km}}{\text{m}^2}$ and P-wave velocity of $V_p = 6.6$ km/s. These values were obtained from a regional gravity survey (Introcaso et al., 1992) and seismic refraction (Barrientos et al., 2004) performed in the southern Andes continental margin. The domain encompassed by the LOFS master faults is referred to as pop-up blocks, which is distinguished from the forearc and backarc host rock by decreasing its Young modulus to 50 GPa. The latter is an attempt to represent its more fractured state due to recurrent faulting, while still behaving elastically at a macroscopic scale. The increased thermal gradient in the volcanic arc, where the pop-up blocks are located, also supports this elastic stiffness reduction, since the value of E diminishes with temperature. We modeled the fault zone using an elastic–plastic constitutive relation, following a von-Mises yield criteria as defined in Equation 2-6 and Equation 2-7. Similar approaches can be found in Regenauer-Lieb & Yuen, (1998), Hardacre & Cowie, (2003). Its elastic properties are equal to those of the pop-up blocks. The values of τ_0 and τ_∞ were set to 20 MPa and 8 MPa respectively, to represent the range of experimentally deformed mylonites (White et al., 1980). The hardening exponential rate β was set to 100, intended to modulate the quick asymptotic behavior of τ_y between $\underline{\varepsilon}^p = 0$ and 0.05.

Steady-state loading was employed to represent the long-term deformation of the LOFS. This assumption is supported by the fact that we include in the geometry a developed shear zone, without considering its genesis. The model's boundary conditions were represented by an imposed velocity on its western surface simulating plate convergence. Linear springs of high stiffness were placed as a lateral constraint, reproducing the roughly null velocity condition caused by the entire South-American plate weight to the west, but neglecting stress concentration on the model's edges. The overburden pressure was simulated by weight body forces in each element and an uniform pressure on the model's top surface. Linear springs were attached to the bottom of the model to simulate the buoyancy effect of the underlying lower crust and mantle. Northern and southern free edges were laterally loaded according to the overburden pressure at the modeled depth.

Since this is a 3D model, uplifting of the pop-up blocks should naturally occur in the interior of the analyzed domain. Whereas vertical stress and infinitesimal strain are modeled properly, fault dip-slip may be overestimated. This is because strain should be integrated through depth of the entire fault system geometry (e.g. splay faults in the brittle domain (Figure 2-2)), which is beyond the scope of this work.

The model constructed here is intended to represent the inter-seismic phase of the subduction seismic cycle, when most of the permanent long-term geological deformation is achieved. One obvious limitation of this approach is that the region under study is currently in the post-seismic phase of the 1960 $Mw = 9.5$ Valdivia earthquake (Wang et al., 2007; Moreno et al., 2011). However, with our model we do not intend to reproduce the short-term current state of stress of the upper plate following any given earthquake, but instead we address the long-term state of stress in an obliquely converging continental margin in general.

The model setup also implies full interplate coupling throughout the subduction boundary. Again, this is a strong assumption as it is well known that current plate coupling is not only partial, but heterogeneously distributed across and along the plate interface (Moreno et al., 2011; Métois et al., 2012). Consistently with what we stated in the paragraph above, our model does not seek to reproduce the state of stress arising from the current nature of plate coupling, but for the more general, simple case, of homogeneous full plate coupling. One consequence of this is that our model will not necessarily reproduce the present-day state of stress at any given point, nor the exact slip-rate magnitudes, but rather the long-term general nature and spatial distribution of stresses along and across the continental margin.

After the mesh was generated, and the boundary conditions and loads were defined, we solved the set of nonlinear equations that depend on the nodal displacement values

deforming the mesh grid. To this end, we used an enhanced version of FEAP 8.4.1.d, which uses iterative non-linear solvers to compute the nodal displacements. Post-processing data to generate stress and strain fields was performed using Paraview 4.0.1.

2.4 Results

The maximum and minimum compressional principal-stress axes orientation, σ_1 and σ_3, respectively, are shown as crosses in Figure 2-4. An overall transpressional–compressional regime is generated within the domain of analysis, with horizontal σ_1 trending from ESE–WNW to NE–SW. The principal orientations are heterogeneously oriented across and along the continental margin, having a strong dependence upon the rheological domain. In general, σ_1 orientations are not parallel to the convergence vector, but clockwise rotated outside the duplex faults and counter-clockwise rotated within them. Clockwise rotation attains 5° to 19° in the forearc and backarc domains, with an average value of 12°. Counter-clockwise rotations can attain as much as 25° in the master faults. The eastern master fault displays a more oblique orientation of σ_1 than that of its western counterpart. Secondary faults exhibit a σ_1 orientation of 0° to -12° with respect to the convergence vector.

As with σ_1, σ_3 axis orientations are mostly horizontal in the duplex faults (with the exception of the western master fault, where it becomes oblique as it extends to the north). This indicates an overall strike-slip stress state. In contrast, σ_3 orientations are mostly vertical in the forearc and pop-up blocks, indicating a compressional regime. Comparatively, σ_3 orientations become horizontal in the foreland, up to 50 km east from the duplex, beyond which its orientation progressively returns to the vertical. No significant differences in σ1 and σ3 axes orientations spatial distribution are yielded in the equivalent 15 km-depth model.

We characterize stress relative magnitudes using the stress shape ratio, which is an adimensional parameter defined as

$$\phi = \frac{\sigma_2 - \sigma_3}{\sigma_1 - \sigma_3}$$ **Equation 2-8**

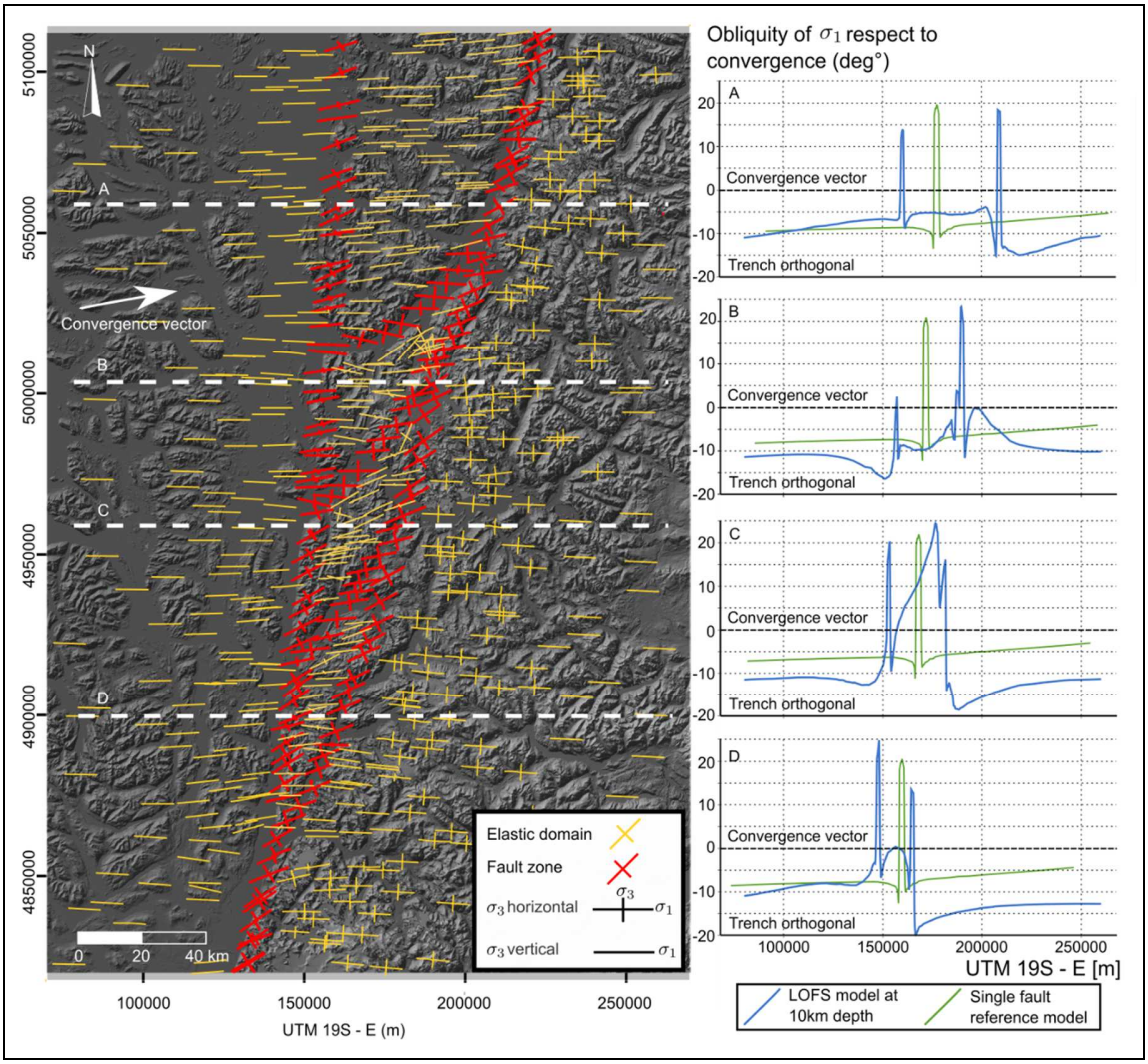

Figure 2-4: Maximum (σ_1) and minimum (σ_3) principal stress orientations are projected as crosses to a horizontal plane at 10 km depth, where the large lines represents σ_1 and the small line represents σ_3. Given that σ_3 is not always horizontal, a strike-slip stress regime is exhibited when the full cross is plotted and a compressional regime is attained when only σ_1 is displayed. An oblique orientation

(between the horizontal plane and the vertical axis) is attained where σ_3 is partially displayed. Red and yellow crosses represent the stress orientations within the fault system and over the outer/inner blocks, respectively. Segmented white line transects are displayed on the map, on which the obliquity of σ_1 orientation is plotted with respect to the convergence vector (N80°E).

where σ_i denotes the i-th principal stress (i = 1, 2, 3) of the Cauchy stress tensor. The stress shape ratio enables contrast of different stress styles, such as the transtensional and transpressional states in a strike-slip context. A schematic representation of ϕ is shown in Figure 2-5, explaining its associated stress states using the Mohr's circle.

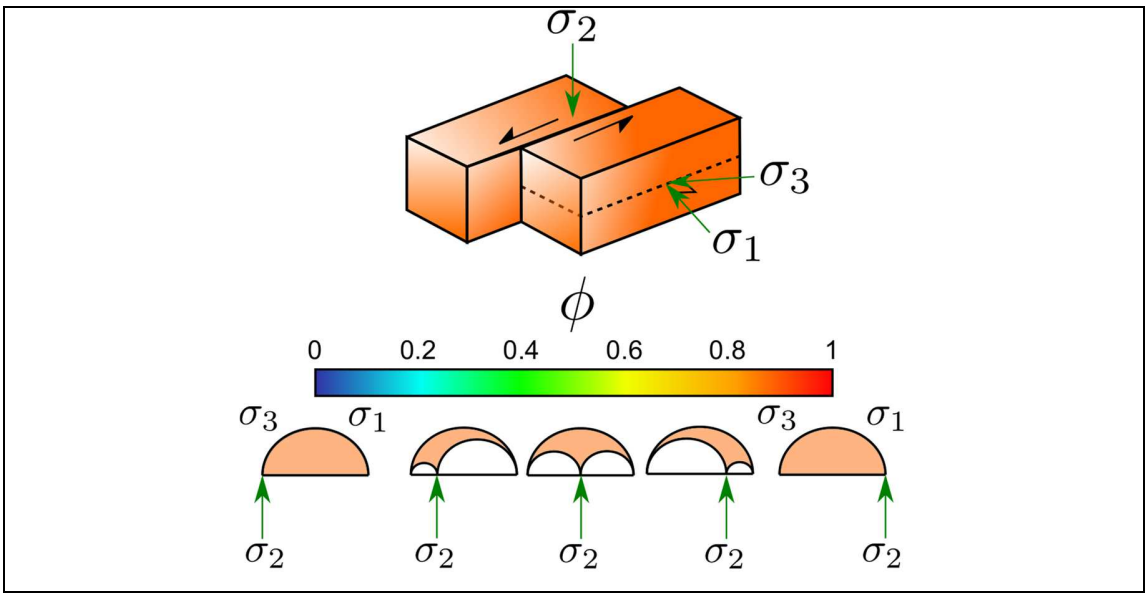

Figure 2-5: Graphical representation of the stress shape ratio in an overall strike-slip regime. Values of $\phi = 0$ indicate uniaxial compression, $\phi = 0.6$ pure strike slip and $\phi = 1$ implies uniaxial extension. Transpression and transtension are located between those values, respectively.

The modeled stress shape ratio ϕ, at two depths of 10 km and 15 km, is shown in Figure 2-6. In the 10 km-depth model, transpressional stress dominates the western master fault (with average values of$\phi = 0.2$), whereas pure strike-slip is shown in the eastern master fault (with ranging values of 0.5). A transtensional-to-extensional regime is produced in

secondary NE striking faults, with a tendency towards strike-slip from south to north. In the 15 km-depth model the eastern master fault becomes more transpressional, whereas the western master fault becomes compressional. Secondary NE-striking faults transtensional domains become smaller than those of the 10 km-depth model. Their general stress state at the 15 km-depth model is strike-slip-to-transpressional.

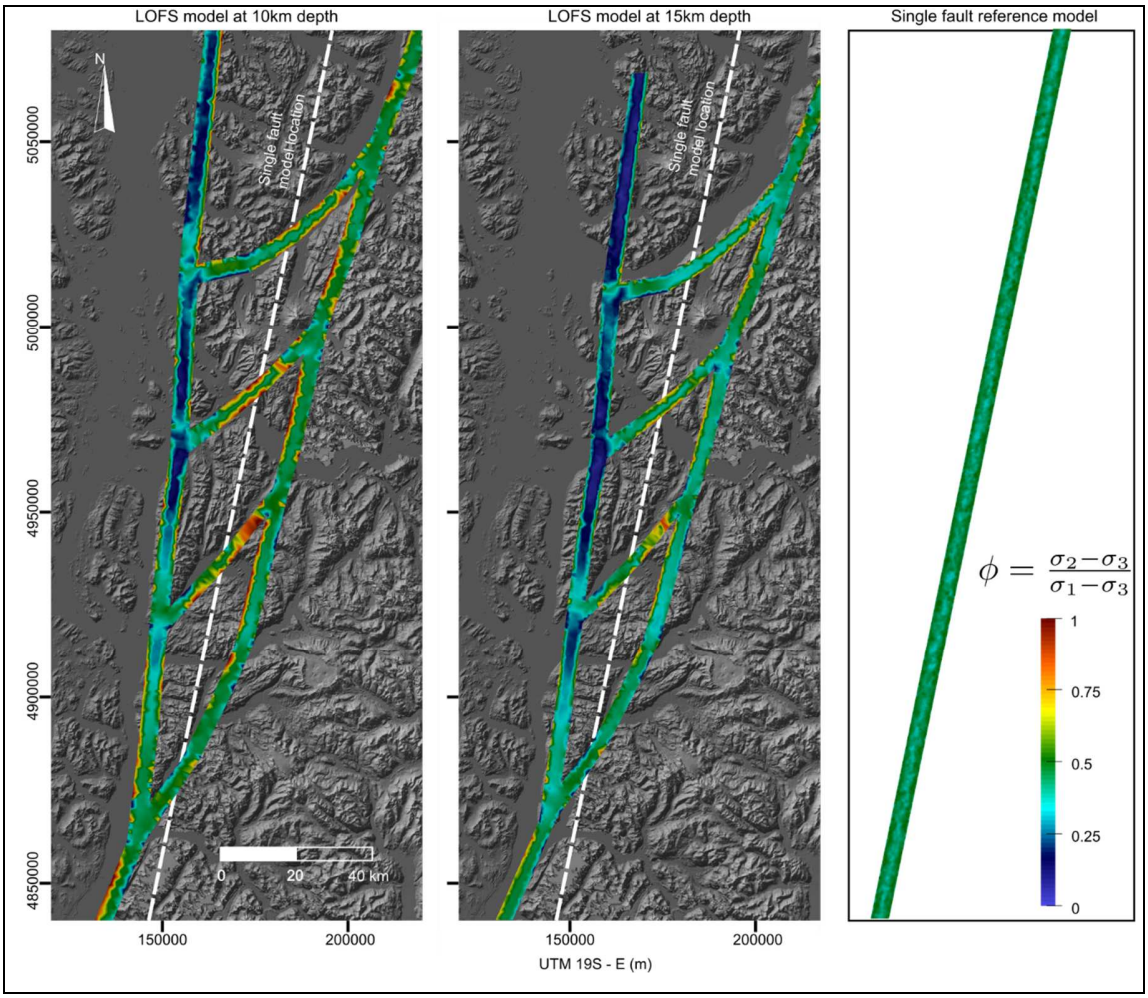

Figure 2-6: Spatial distribution of the stress shape ratio throughout the fault system at 10 km depth and 15 km depth. It is also plotted for the single fault reference model.

The modeled slip rate within the different faults making up the duplex is calculated using the relative velocities of two small parallel segments, which face each other from both sides of the duplex fault under consideration. The slip rate field in [mm/yr] of the LOFS is plotted in Figure 2-7. Fault segments display markedly different slip rates: The single southernmost segment has significant greater slip rate than the rest. It is followed in decreasing order of slip rate, by the eastern master fault and the secondary faults, and then the western master fault segment. The slip rate of the eastern master fault slightly increases northward, whereas the western master fault and secondary faults decrease in slip rate towards the north. In contrast, the single fault model displays an uniform slip rate of 16.6 mm/yr.

2.5 Discussion

2.5.1 Geological scope of the model

To model the deformation mechanisms within the entire fault zone, we make an effort to constrain the internal bulk plasticity of the rock volume rather than considering each individual shear band as a surface of discontinuity, such as in dislocation type models (e.g. Stanton-Yonge et al., 2016; Provost et al., 2003). Approaches similar to ours can be found in models of fabric development with prescribed plastic shear bands, using a von-Mises yield criterion to simulate dislocation glide (e.g. Schmalholz & Maeder, 2012), which is pressure independent. Furthermore, our approach gives the outstanding advantage to account for the compartmentalization of stress and strain within the fault zone, rather than its localization in a discrete fault plane, which is not geologically accurate when representing the brittle–plastic transition. Another approach to model a fault zone consists in defining elastic volumes with reduced Young's modulus, which neglect permanent deformation produced by plastic flow (Karaoğlu et al., 2016). Since no yield stress limit is imposed in this method, it overestimates the stress field magnitude as it ignores the stress release when the fault zone slips (i.e. the stress strongly depends on the time of loading).

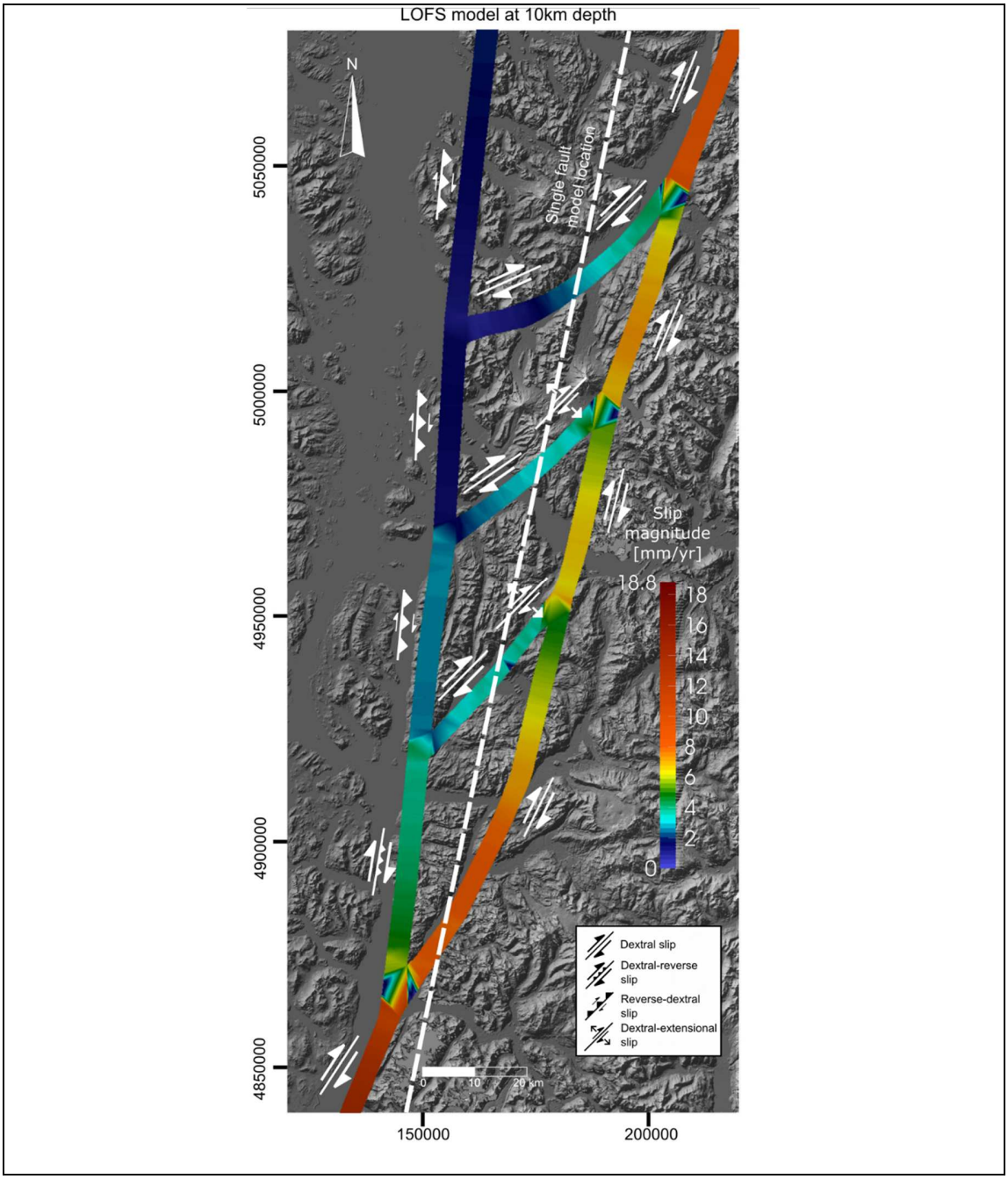

Figure 2-7: Fault slip rate at master and subsidiary LOFS duplex faults. Slip rates within the duplex structures range from 1 to 10 mm per yr. The maximum slip rate is located in the southernmost single segment. The single fault model displays an uniform slip rate of 16.6 mm per yr. The overall kinematics of the duplex fault segments is displayed alongside.

Permanent deformation in a fault zone is possible due to crystal–plastic slip systems, which is the main deformation mechanism in the brittle–plastic transition for quartz-rich rocks (Hirsch & Roberts, 1997; Hirth & Tullis, 1992), coexisting with micro-fracturing and pressure solution. We use a continuum approximation and a distributed plastic material model, characterized by a von-Mises criterion with isotropic strain-hardening. This is generally a common approach to model the brittle–plastic transition deformation mechanisms in shear zones, as suggested by Mancktelow, (2006) and Regenauer-Lieb & Yuen, 2003. However, there is a current uncertainty in the precise geometry of mylonitic shear bands throughout the fault system, along with the spatial distribution of its thermodynamic state (e.g. horizontal distribution of temperature, which activates plastic mechanisms). Therefore, we propose that the use of Von-Mises continuum plasticity approach is reasonable, given that it is able to reflect the average behavior of the fault zone. Its associated flow law allows strain to localize in the maximum shear stress direction, in contrast to a Mohr–Coulomb criterion. More complex constitutive relations can be used in future efforts, such as multi-scale plasticity models embedded in FE simulations (Hurtado & Ortiz, 2013), to account for dislocation, micro-fracturing and grain boundary deformation mechanisms, with the aim of achieving a more complete understanding of the fault zone behavior (Kohlstedt & Evans, 1995).

Previous efforts to study the LOFS stress field, such as in Islam, (2009), considered fault zones as individual lines in 2D models by using a Mohr–Coulomb yield criterion. Therefore, it produces a highly discontinuous stress and strain fields throughout the fault zone vicinity. However, mylonitic shear bands are distributed within a large width in contrast to a discrete plane, as can be seen in Cembrano et al. (2002). Also, in numerical simulations of obliquely convergent plate boundaries (e.g. Braun and Beaumont, 1995), deformation localizes in wide shear zones within a transpressional tectonic regime.

2.5.2 Consistency between the model and geological/seismic observations

To assess the validity, advantages and limitations of the proposed model, we compare our results with field data found in the literature (Figure 2-8). Specifically, we confront our results with fault slip data inversions and crustal seismicity obtained from local and/or regional networks (Arancibia et al., 1999; Lange et al., 2008; Legrand et al., 2011). We highlight that both data sources are restricted to the brittle portion of the lithosphere. However, the brittle domain of a fault zone should slip as a response to the flow of the stronger brittle–plastic transition domain (Mancktelow, 2006), where the localization or distribution of brittle fracturing strongly depend on the underlying lithosphere low or high viscosity, respectively (Schueller et al., 2005). Therefore, if we consider long-term deformation, comparing the model stress state with fault slip data and crustal seismicity should be valid as a first order approximation, given that individual faults respond to the fault zone stress calculated in this model.

To confront our model with available seismic data, we project the 10 km-depth modeled stress tensor on the nodal plane solution evaluated for three representative seismic events. To this end, we compute the modeled shear stress vector $\boldsymbol{\tau}$

$$\boldsymbol{\tau} = \boldsymbol{\sigma n} - (\boldsymbol{n} \cdot \boldsymbol{\sigma n})\boldsymbol{n} \qquad \textbf{Equation 2-9}$$

where $\boldsymbol{\sigma}$ is the modeled stress tensor and $\boldsymbol{n}$ is the nodal plane solution in the seismic events. Projecting $\boldsymbol{\tau}$ onto the slip $\boldsymbol{s}$ recorded in an earthquake at the location of its nucleation, we calculate the misfit angle between both vectors (Table 2-1). A small misfit of 4° to 12° is confirmed for the three seismic events studied.

Table 2-1: Comparison between seismic data (Lange et al., 2008; Legrand et al., 2011) and model results. Vectors are given in azimuth/plunge degrees.

Site	Seismic data (s)	Model results (τ)	Missfit (°)
A	129/45	145/43	12
B	179/09	173/18	9.4
C	191/22	189/19	4

Following this, we compare the 10 km-depth modeled stresses with the paleostress inversion from structural field measurements. It is important to remark that both our model and fault slip inversions describe the long-term averaged stress during a certain tectonic period. We calculate the misfit between paleostress inversion and modeled σ_1 orientations and ϕ values (Table 2-2). The similar values observed indicate that the bulk stressing on the fault zone calculated in this model is capable and sufficient to approximately reproduce the state of stress ellipticity on shallower portions of the crust. Moreover, it also suggests that the stress regime has not changed much since the brittle deformation took place, that is from 1.6 Ma (Lavenu and Cembrano, 1999).

Table 2-2: Comparison between observed data in paleostress inversions performed by Arancibia et al. (1999) and modeled data. The model results were averaged within a range of 500 m of the paleostress inversion site location and the paleostress inversion was averaged considered the number of fault planes measured in-situ.

Site	σ_1 orientation			ϕ value		
	Paleostress inversion	Model	Missfit	Paleostress inversion	Model	Difference of averages
1	087/01	070/00	15.7	0.03-0.29	0.42-0.45	-0.299
2	096/12	094/04	15.2	0.52-0.54	0.41-0.62	0.017
3	250/07	070/01	8.5	0.3-0.5	0.32-0.45	0.033

Although earthquakes represent an instantaneous event of deformation, we remark that these events (and particularly the Aysén 2007 seismic swarm) nucleated upward from the brittle–plastic transition. Furthermore, there is a low misfit angle (4°–12°) between modeled and seismic slip vectors. This indicates that the model is sufficiently accurate in predicting the deformation and stress styles at the fault zone, regardless of the rheological difference between these structural levels. However, a different stress shape ratio distribution can be observed in the 15 km-depth model (Figure 2-6). Secondary faults exhibit a less extensional-to-transtensional behavior than the 10 km-depth model, being loaded mostly in transtensional-to-strike-slip in the 15 km-depth model. This indicates that the mode of fracturing (and therefore, focal mechanism of earthquakes if they are generated) varies in higher depths of the brittle–plastic transition.

2.5.3 Tectonic insights

As shown in Figure 2-4, the predicted maximum principal stress orientation within the forearc and foreland is not parallel to the convergence vector, but it is clockwise rotated from the convergence vector by 5° to 19°, whereas at the fault zone it is rotated up to 25° counter-clockwise. The results in the fault zone are consistent with analytical solutions for the velocity fields in oblique convergence margins (Teyssier et al., 1995) and geological studies in the northern end of the LOFS (Pérez-Flores et al., 2016), which implies that the oblique component of convergence is mostly accommodated by a margin parallel fault system. In fact, Teyssier et al. (1995) propose that this partitioning is likely due to the convergence velocity and its obliquity rather than the mechanical properties of the lithosphere. However, modeling shear zones without any contrast in elasticity modulus or yield stress would produce a fully non-partitioned stress field. Thus, we conclude that both the spatial distribution of rheological heterogeneities and the convergence velocity/obliquity determine the stress distribution within the continental margin.

Stress states are heterogeneous within different fault segments of the duplex (Figure 2-6), whereas the single fault model under the same boundary conditions and rheological properties displays only a pure strike-slip shearing mode ($\phi \approx 0.5$). Therefore, the orientation of the plastic shear zone plays a key role in how the fault is loaded. The eastern master fault displays stresses close to pure strike-slip shearing mode ($\phi = 0.45 - 0.5$), whereas the western fault loads mostly compressional-to-transpressional shearing mode ($\phi = 0.2$), which is consistent with geomorphologic, block uplifting observations and BEM modeling (Thomson, 2002; Glasser and Ghiglione, 2009; Stanton-Yonge et al., 2016). In fact, the western master fault accommodates the compressional stress arising from convergence, thus allowing the uplifting of the Cordillera at the considered latitude. Also, the disruption of the stress field near a fault intersection, which is caused by the adjacent faults' kinematics must be taken into account. For instance, transtensional-to-extensional behavior of NE-secondary-faults is limited to their easternmost segment, most likely due to the feedback between their kinematics and the eastern master fault strike-slip kinematics. This feedback was also observed in the Aysén seismic swarm where the extensional $M_w = 6.1$ event (A in Figure 2-1) triggered the following strike-slip $M_w = 6.2$ (B in Figure 2-1) event in the eastern master fault (Legrand et al., 2011).

The stress state contrast between the 10 km-model and the 15 km-model can be explained by the change in boundary conditions of the model. The 15 km-model displays, in overall, a stress state shifted towards compressional loading of both the eastern and western master faults. In this scenario, both vertical and NS-trending stress boundary conditions, given by lithostatic pressure, increase in the same magnitude. However, the identical velocity boundary conditions between both models implies that EW-trending stress increases in depth. Since stress is equally magnified for two orthogonal directions (vertical and NS-trending) in depth, it requires a greater stress component in the remaining orthogonal direction (EW-trending) to produce the same level of deformation. In this context, secondary faults diminish their extensional behavior, which is due to the increase of σ_1

(horizontal) versus vertical stress. Furthermore, rotations of the stress tensor in the model are invariant between the two models, given that the faults and boundary condition orientations remain constant. In this regard, the variation in depth of the topography's influence, faults' dip and the relative velocity of the subduction interface, should account for the stress tensor rotation.

Fault slip rates predicted by our analysis are comparable and consistent with similar mechanical models at a larger scale. Whereas BEM models fault zones as discrete surfaces (e.g. Stanton- Yonge et al., 2016), following the theory of angular dislocation in an elastic medium, our model takes into account the inner rheology of fault zones within a given width. It considers that deformation compartmentalizes on the entire fault zone volume. The advantages of the FE model are that we can model with a greater level of detail small-scale geologic features, resulting in more accurate mechanics of fault slip. Further, the consideration of elasto-plastic rheology on the fault zone represents the velocity upper bound expected within the brittle regime of the overlying lithosphere. Although, brittle deformation is partitioned into imbricated discrete faults, each of which should slip at slower rates than their brittle–plastic counterpart.

The slip rate (16.6 mm/yr) calculated in the single fault model is compartmentalized within the LOFS duplex. It can be observed in Figure 2-7 that the southernmost single segment of the LOFS displays a value of 16 mm/yr, which indicates that it sustains most of the equivalent slip of the single-fault model. However, as the duplex extends from south to north, its overall slip rate is shared between both master faults: the slip rate of the eastern master fault increases progressively to the north, whereas that of the western master fault decreases. This observation can be explained by their stress loading mode. The southernmost segment of the western fault is loaded under transpressional-to-strike-slip shearing mode, thus sustaining a significant fraction of the margin-parallel component of the convergence vector. In contrast, the northernmost segment of the westernmost is

loaded in a transpressional-to-compressional shearing mode. This fact, along with its steep dip, suggests that in the north it accommodates only the margin-orthogonal component of the convergence vector. Furthermore, this vertical slip rate of 2 mm/yr could be significant to the pop-up blocks uplifting, and to the orogenesis at this latitude.

It can be observed in Figure 2-7 that the slip rate field is not smooth throughout all of the master faults' segments. Slip rate in the eastern master fault is disrupted by the presence of oblique NE-striking faults. Moreover, the magnitude of the slip rate is higher at the northern segments of fault intersections in contrast to southern segments. This phenomenon can also be explained if we consider the $M_w = 6.1$ and 6.2 events of the Aysén swarm: when the extensional $M_w = 6.1$ event occurred, it displaced the northern block of the fault northward and the southern block southward. Thus, the velocity tendency is greater in the northern block (where the following $M_w = 6.2$ took place), given that its velocity superimposes on the dextral kinematics of the eastern master fault. On the other hand, the southern block southward velocity is in opposite sense to the eastern fault dextral kinematics. This would account for a greater overall slip rate northward of the fault intersection within the eastern master fault, rather than southward. Therefore, this example can account for the influence of coupled kinematics at adjacent fault segments on their slip rates along strike. This can be observed at Figure 2-7 in the eastern master fault, where the slip rate diminishes as it moves north towards a fault intersection with a secondary NE-striking fault, then increasing again as it progresses away northward. Next to a fault intersection, the slip is enhanced in the fault segment in which both tectonic loading and the stressing caused by slip in the same sense along an adjacent fault.

Regarding the seismicity recorded in the fault system, we highlight the consistency between the focal mechanisms, the recorded slip vector (Legrand et al., 2011), and the stress state predicted by the model (Table 2-1). We note that these results correspond to different depths: the hypocenter depth of the $M_w = 6.2$ event (focal mechanism B in

Figure 2-8) was 4 km and the model was produced at 10 km. This is consistent with a brittle–plastic transition that drives the stress state of the seismogenic region.

2.5.4 Magma transport

When comparing to the volcano-tectonic $M_w = 6.1$ event (focal mechanism A in Figure 2-8), our numerical model results show great consistency with its stress state. Transtensional-to-extensional stress is clear within the NE-striking fault responsible for the event. The Aysén seismic swarm was recorded from a maximum depth of 8.3 km and the event A occurred at a depth of 5.3 km (Legrand et al., 2011). Moreover, the entire seismic swarm is representative of magma upward migration from the brittle–plastic transition, with fault-plane solutions that can be caused by both tectonic stress and dyke inflation. These solutions often differ considerably depending on the regional tectonic setting and the magma–wall rock interaction (Roman & Cashman, 2006). On the other hand, our model captures the stress state due to the long-term behavior of the fault system, therefore immediately before magma was transported upward. Given the model's consistent results, we propose that NE-striking faults, close to the intersection with the eastern master fault, serve as long-lived magma pathways, maintained by tectonic loading conditions. This is supported by the existence of volcanos Maca and Cay, which are approximately placed on NE-striking faults, along with several monogenetic cones (Legrand et al., 2011).

Furthermore, we calculate the fluid overpressure ratio λ required to slip given a fault's orientation, which is the percentage of fluid pressure against lithostatic vertical stress. Particularly, we seek the lower boundary of λ where slip is associated with extension in brittle faulting, either in Mode I or in Mode II fracturing. Mode I alone would require greater values of λ. Following the scheme provided in Roquer et al., (2017) and references therein, λ can be obtained by rewriting the Murrel's expansion of Griffith criterion (generalized Griffith criterion) in terms of the fluid overpressure ratio λ, the normal stress

$\sigma_n = \boldsymbol{n} \cdot \boldsymbol{\sigma n}$ and the shear stress magnitude $\tau = ||\boldsymbol{\tau}||$, projected on the nodal planes of the M_w event:

$$\lambda = \frac{P_f}{\sigma_v} = \frac{\sigma_n + T}{\rho g z} + \frac{\tau^2}{4 T \rho g z} \qquad \textbf{Equation 2-10}$$

where P_f is the fluid pressure, σ_v the vertical loading and T the tensile strength of the rock, assumed to be equal to 4 MPa (Gudmundsson, 2011). For the NE-striking fault, the minimum value of λ is 0.83, which indicates that a magma pressure equals to at least 0.83 times the value of lithostatic vertical stress is needed to produce extension, and therefore a pathway for magma upward migration. Regarding this observation, the tectonic conditions are sufficient to develop local extension for magma to migrate upwards, with no particular assistance of magma overpressure. However, this may be an oversimplified statement because a mechanically coupled feedback between overpressure and tectonic loading should usually exist. Furthermore, the link between magmatism and fault development is addressed in other works using distributed plasticity and hydro-mechanical feedback (e.g. Gerbault et al., 2012), in which magma pressure assists fault nucleation. Consequently, shear zones localization assists magma upward migration. Given that we use a non-coupled hydro-mechanical approach, an improved comprehension between tectonics and magmatism can be used in future work by integrating this feedback. On the other hand, relatively large areas of extension are observed by the model (4–10km^2), implying that large volumes of magma could be transported up through the brittle–plastic transition, perhaps using micro-cracks pathways within mylonites (Bauer et al., 2000; Handy & Streit, 1999).

Aside from the fault where the $M_w = 6.1$ event was generated, extensional behavior also occurs on the secondary fault zone edges, as well as in other regions of the eastern master fault. This observation could provide evidence for self-similarity between crystal–plastic mechanisms and tectonic macro-behavior, given that dilatant micro-fractures are often

found within plastic shear zones boundaries. These fractures precede plastic deformation (Segall & Simpson, 1986) and serve as fluid pathways, consequently being obliterated by excessive deformation when the shear zone grows. We plan to achieve a better comprehension of such coupled phenomena in the future by dealing faults with a dynamic geometry, within the context of multi-scale plasticity models.

2.6 Conclusions

- Our model shows that the maximum principal stress (σ_1) orientation varies along and across strike of the continental margin. In the forearc and backarc domains, σ_1 is clock-wise rotated with respect to the convergence vector (ca. 15°), whereas it is slightly counter-clockwise rotated along the duplex master faults (15°–25°). This is consistent with continental-scale slip partitioning. Fault slip rates also vary along and across strike. The duplex eastern master fault slip rates range from 7 to 10 mm/yr (increasing northward), whereas the western master fault slip ranges from 1 to 4 mm/yr (decreasing northward). Secondary NE-striking faults show slip rates up to 3 [mm/yr].
- Different branches of the LOFS differ significantly in their stress states. The eastern master fault accommodates simple shearing, with ϕ values ranging from 0.45 to 0.5, whereas the western master fault undergoes mostly pure shearing, with $\phi \approx 0.2$. Secondary NE-striking faults exhibit transtensional-to-extensional stress regimes with ϕ values ranging from 0.75 to 0.9, being the most favorable faults for magma migration, particularly close to the intersection with the eastern master fault.
- Secondary NE-striking faults of the LOFS duplex exhibit transtensional-extensional stress regimes when they are close to the eastern master fault, and not along their entire extent. Also, a fault segment will have higher slip rate in regions where both tectonic loading and local kinematics favor a compatible slip sense.

- Model results (stress orientation, ellipticity and spatial distribution) are consistent with long-term geologic observations at the outcrop scale, short-term crustal seismicity and regional tectonics in the Southern Volcanic Zone. This shows the potential of FE models to reproduce natural tectonic processes, and more importantly, demonstrates that geological and geophysical observations can be accounted for by a small number of key first order boundary conditions.

2.7 Acknowledgements

This work has been funded by project FONDECYT 1141139 to José Cembrano and FONDAP project 15090013 "Andean Geothermal Centre of Excellence" (CEGA). JC also acknowledges support from FONDAP project 15110017 "National Research Center for Integrated Natural Disaster Management" (CIGIDEN). The authors are grateful Tomás Roquer and Gloria Arancibia for early reviews, Gonzalo Yáñez for useful geophysical insights and Pamela Pérez-Flores, Rodrigo Gomila and Sebastián Castro for geological and computational mechanics discussions. Thorough and constructive reviews by Muriel Gerbault and an anonymous reviewer significantly improved the scientific quality of our manuscript.

REFERENCES

Angermann, D., Klotz, J., & Reigber, C. (1999). Space-geodetic estimation of the nazca-south america euler vector. *Earth and Planetary Science Letters*, *171*(3), 329–334. https://doi.org/10.1016/S0012-821X(99)00173-9

Arancibia, G., Cembrano, J., & Lavenu, A. (1999). Transpresión dextral y partición de la deformación en la Zona de Falla Liquiñe-Ofqui, Aisén, Chile (44-45ºS). *Revista Geológica de Chile*. Retrieved from http://www.scielo.cl/scielo.php?script=sci_arttext &pid=S0716-02081999000100001

Argus, D., Gordon, R., & DeMets, C. (2011). Geologically current motion of 56 plates relative to the no-net-rotation reference frame. *Geochemistry, Geophysics,*. Retrieved from http://onlinelibrary.wiley.com/doi/10.1029/2011GC003751/full

Argus, D., Gordon, R., Heflin, M., & Ma, C. (2010). The angular velocities of the plates and the velocity of Earth's centre from space geodesy. *Geophysical Journal*. Retrieved from http://onlinelibrary.wiley.com/doi/10.1111/j.1365-246X.2009.04463.x/full

Barrientos, S., Vera, E., Alvarado, P., & Monfret, T. (2004). Crustal seismicity in central Chile. *Journal of South American Earth Sciences*, *16*(8), 759–768. https://doi.org/ 10.1016/j.jsames.2003.12.001

Bauer, P., Palm, S., & Handy, M. R. (2000). Strain localization and fluid pathways in mylonite: Inferences from in situ deformation of a water-bearing quartz analogue (norcamphor). *Tectonophysics*, *320*(2), 141–165. https://doi.org/10.1016/S0040-1951(00) 00065-2

Beck, M. (1983). On the mechanism of tectonic transport in zones of oblique subduction. *Tectonophysics*. Retrieved from http://www.sciencedirect.com/science/article/pii/004 0195183902305

Blanquat, M. D. Saint, & Tikoff, B. (1998). Transpressional kinematics and magmatic arcs. *Geological Society,*. Retrieved from http://sp.lyellcollection.org/content/135/1/327.short

Braun, J., & Beaumont, C. (1995). Three-dimensional numerical experiments of strain partitioning at oblique plate boundaries: Implications for contrasting tectonic styles in the southern Coast Ranges, California, and central South Island, New Zealand. *Journal of Geophysical Research: Solid Earth*, *100*(B9), 18059–18074. https://doi.org/10.1029/95JB01683

Carter, N. (1976). Steady state flow of rocks. *Reviews of Geophysics*. Retrieved from http://onlinelibrary.wiley.com/doi/10.1029/RG014i003p00301/full

Cembrano, J., Hervé, F., & Lavenu, A. (1996). The Liquiñe Ofqui fault zone: a long-lived intra-arc fault system in southern Chile. *Tectonophysics*, *259*(1–3), 55–66. https://doi.org/10.1016/0040-1951(95)00066-6

Cembrano, J., & Lara, L. (2009). The link between volcanism and tectonics in the southern volcanic zone of the Chilean Andes: A review. *Tectonophysics*, *471*(1–2), 96–113. https://doi.org/10.1016/j.tecto.2009.02.038

Cembrano, J., Lavenu, A., Reynolds, P., Arancibia, G., López, G., & Sanhueza, A. (2002). Late Cenozoic transpressional ductile deformation north of the Nazca–South America–Antarctica triple junction. *Tectonophysics*, *354*(3–4), 289–314. http://dx.doi.org/10.1016/S0040-1951(02)00388-8

Cembrano, J., & Moreno, H. (1994). Geometría y naturaleza contrastante del volcanismo Cuaternario entre los 38 S y 46 S: Dominios compresionales y tensionales en un régimen transcurrente. *Congreso Geológico Chileno*. Retrieved from http://biblioserver.sernageomin.cl/opac/DataFiles/7166pp240_244.pdf

Chapman, D. (1986). Thermal gradients in the continental crust. *Geological Society, London, Special*. Retrieved from http://sp.lyellcollection.org/content/24/1/63.short

Cox, S. F. (2010). The application of failure mode diagrams for exploring the roles of fluid pressure and stress states in controlling styles of fracture-controlled permeability enhancement in faults and shear zones. *Geofluids*, 217–233. https://doi.org/10.1111/j.1468-8123.2010.00281.x

DeMets, C., Gordon, R. G., & Argus, D. F. (2010). Geologically current plate motions. *Geophysical Journal International*, *181*(1), 1–80. https://doi.org/10.1111/j.1365-246X.2009.04491.x

Faulkner, D., Jackson, C., & Lunn, R. (2010). A review of recent developments concerning the structure, mechanics and fluid flow properties of fault zones. *Journal of Structural*. Retrieved from http://www.sciencedirect.com/science/article/pii/S01918141100010 1X

Gerbault, M., Cappa, F., & Hassani, R. (2012). Elasto-plastic and hydromechanical models of failure around an infinitely long magma chamber. *Geochemistry, Geophysics,*. Retrieved from http://onlinelibrary.wiley.com/doi/10.1029/2011GC003917/full

Glasser, N. F., & Ghiglione, M. C. (2009). Structural, tectonic and glaciological controls on the evolution of fjord landscapes. *Geomorphology*, *105*(3–4), 291–302. https://doi.org/10.1016/j.geomorph.2008.10.007

Gudmundsson, A. (2011). *Rock fractures in geological processes*. Retrieved from https://books.google.cl/books?hl=en&lr=&id=Zup8fBHpBpwC&oi=fnd&pg=PR5&dq=gudmunsson+rock+fractures+in+geological+processes&ots=Ho9u7DX5Eb&sig=hd5lrbq7dAUuhtWn3CtbSV0biZI

Guineberteau, B., & Bouchez, J. (1987). The Mortagne granite pluton (France) emplaced

by pull-apart along a shear zone: Structural and gravimetric arguments and regional implication. *Geological Society of*. Retrieved from http://gsabulletin.gsapubs.org/content/99/6/763.short

Handy, M. R., & Streit, J. E. (1999). Mechanics and mechanisms of magmatic underplating; inferences from mafic veins in deep crustal mylonite. *Earth and Planetary Science Letters*, *165*(3–4), 271–286. https://doi.org/10.1016/S0012-821X(98)00272-6

Hardacre, K., & Cowie, P. (2003). Variability in fault size scaling due to rock strength heterogeneity: a finite element investigation. *Journal of Structural Geology*. Retrieved from http://www.sciencedirect.com/science/article/pii/S0191814102002055

Heidbach, O., Tingay, M., Barth, A., Reinecker, J., & Kurfeß, D. (2010). Global crustal stress pattern based on the World Stress Map database release 2008. *Tectonophysics*. Retrieved from http://www.sciencedirect.com/science/article/pii/S0040195109004132

Hervé, F. (1993). Paleozoic metamorphic complexes in the Andes of Aysén, southern Chile (West of Occidentalia). *Proceedings of the First Circum-Pacific and Circum-*. Retrieved from https://scholar.google.cl/scholar?q=herve+paleozoic+metamorphic+complexes+in+the+andes&btnG=&hl=en&as_sdt=0%2C5

Hirsch, P. B., & Roberts, S. G. (1997). Modelling plastic zones and the brittle-ductile transition. *Philosophical Transactions of the Royal Society A: Mathematical, Physical and Engineering Sciences*, *355*(1731), 1991–2002. https://doi.org/10.1098/rsta.1997.0101

Hirth, G., & Tullis, J. (1992). Dislocation creep regimes in quartz aggregates. *Journal of Structural Geology*. Retrieved from http://www.sciencedirect.com/science/article/pii/019181419290053Y

Hubbert, M., & Rubey, W. (1959). Role of fluid pressure in mechanics of overthrust faulting I. Mechanics of fluid-filled porous solids and its application to overthrust faulting.

Geological Society of America. Retrieved from http://gsabulletin.gsapubs.org/content/70/2/115.short

Hurtado, D., & Ortiz, M. (2013). Finite element analysis of geometrically necessary dislocations in crystal plasticity. *International Journal for Numerical*. Retrieved from http://onlinelibrary.wiley.com/doi/10.1002/nme.4376/full

Hutton, D. (1988). Granite emplacement mechanisms and tectonic controls: inferences from deformation studies. *Transactions of the Royal Society of*. Retrieved from http://journals.cambridge.org/abstract_S0263593300014255

Hutton, D. H. . (1982). *A method for the determination of the initial shapes of deformed xenoliths in granitoids*. *Tectonophysics* (Vol. 85). Elsevier. https://doi.org/10.1016/0040-1951(82)90100-7

Introcaso, A., Pacino, M., & Fraga, H. (1992). Gravity, isostasy and Andean crustal shortening between latitudes 30 and 35 S. *Tectonophysics*. Retrieved from http://www.sciencedirect.com/science/article/pii/0040195192904164

Islam, M. (2009). Origin of the regional stress field along the Liquine-Ofqui Fault Zone (LOFZ), Southern Chilean Andes by means of FE simulation. *Journal of Mountain Science*. Retrieved from http://www.springerlink.com/index/RJ631Q668504826L.pdf

Jensen, E., Cembrano, J., Faulkner, D., Veloso, E., & Arancibia, G. (2011). Development of a self-similar strike-slip duplex system in the Atacama Fault system, Chile. *Journal of Structural Geology*, *33*(11), 1611–1626. https://doi.org/10.1016/j.jsg.2011.09.002

Karaoğlu, Ö., Browning, J., & Bazargan, M. (2016). Numerical modelling of triple-junction tectonics at Karlıova, Eastern Turkey, with implications for regional magma transport. *Earth and Planetary*. Retrieved from http://www.sciencedirect.com/science/article/pii/S0012821X16303934

Kendrick, E., Bevis, M., Smalley, R., & Brooks, B. (2003). The Nazca–South America Euler vector and its rate of change. *Journal of South*. Retrieved from http://www.sciencedirect.com/science/article/pii/S0895981103000282

Kohlstedt, D., & Evans, B. (1995). Strength of the lithosphere: Constraints imposed by laboratory experiments. *Journal of Geophysical*. Retrieved from http://onlinelibrary. wiley.com/doi/10.1029/95JB01460/full

Lahsen, A. (1988). Chilean geothermal resources and their possible utilization. *Geothermics*.

Lange, D., Cembrano, J., Rietbrock, A., Haberland, C., Dahm, T., & Bataille, K. (2008). First seismic record for intra-arc strike-slip tectonics along the Liquiñe-Ofqui fault zone at the obliquely convergent plate margin of the southern Andes. *Tectonophysics*, *455*, 14–24. https://doi.org/10.1016/j.tecto.2008.04.014

Lara, L. E., Cembrano, J., & Lavenu, a. (2008). Quaternary Vertical Displacement along the Liquiñe-Ofqui Fault Zone: Differential Uplift and Coeval Volcanism in the Southern Andes? *International Geology Review*, *50*(11), 975–993. https://doi.org/10.2747/0020-6814.50.11.975

Lavenu, a, & Cembrano, J. (1999). Compressional and transpressional stress pattern for the Pliocene and Quaternary (Andes of central and southern Chile). *Journal of Structural Geology*, *21*, 1669–1691. https://doi.org/10.1016/S0191-8141(99)00111-X

Legrand, D., Barrientos, S., Bataille, K., Cembrano, J., & Pavez, A. (2011). The fluid-driven tectonic swarm of Aysen Fjord, Chile (2007) associated with two earthquakes (Mw=6.1 and Mw=6.2) within the Liquiñe-Ofqui Fault Zone. *Continental Shelf Research*, *31*(3–4), 154–161. https://doi.org/10.1016/j.csr.2010.05.008

Mancktelow, N. (2006). How ductile are ductile shear zones? *Geology*. Retrieved from

http://geology.gsapubs.org/content/34/5/345.short

McCaffrey, R. (1992). Oblique plate convergence, slip vectors, and forearc deformation. *Journal of Geophysical Research: Solid Earth*. Retrieved from http://onlinelibrary. wiley.com/doi/10.1029/92JB00483/full

McClay, K. (1977). Pressure solution and Coble creep in rocks and minerals: a review. *Journal of the Geological Society*. Retrieved from http://jgs.lyellcollection.org /content/134/1/57.short

Melnick, D., Folguera, A., & Ramos, V. A. (2006). Structural control on arc volcanism: The Caviahue–Copahue complex, Central to Patagonian Andes transition (38°S). *Journal of South American Earth Sciences*, *22*(1–2), 66–88. https://doi.org/10.1016 /j.jsames.2006.08.008

Métois, M., Socquet, A., & Vigny, C. (2012). Interseismic coupling, segmentation and mechanical behavior of the central Chile subduction zone. *Journal of Geophysical*. Retrieved from http://onlinelibrary.wiley.com/doi/10.1029/2011JB008736/full

Molnar, P. (1983). Average regional strain due to slip on numerous faults of different orientations. *Journal of Geophysical Research: Solid Earth*. Retrieved from http://onlinelibrary.wiley.com/doi/10.1029/JB088iB08p06430/full

Moreno, M., Melnick, D., Rosenau, M., & Bolte, J. (2011). Heterogeneous plate locking in the South–Central Chile subduction zone: Building up the next great earthquake. *Earth and Planetary*. Retrieved from http://www.sciencedirect.com/science/article/pii/S00128 21X11001695

Nakamura, K., Jacob, K. H., & Davies, J. N. (1977). Volcanoes as possible indicators of tectonic stress orientation - Aleutians and Alaska. *Pure and Applied Geophysics PAGEOPH*, *115*(1–2), 87–112. https://doi.org/10.1007/BF01637099

Neto, E. de S., Peric, D., & Owen, D. (2011). *Computational methods for plasticity: theory and applications*. Retrieved from https://books.google.cl/books?hl=en&lr=&id=21Q0oLGFZuoC&oi=fnd&pg=PT7&dq=de+souza+netO+computational&ots=CPwDreCRZg&sig=pr5Lao_-5Wp-u60VrSKrqRx1zjM

Pérez-Flores, P., Cembrano, J., & Sánchez-Alfaro, P. (2016). Tectonics, magmatism and paleo-fluid distribution in a strike-slip setting: Insights from the northern termination of the Liquiñe–Ofqui fault System, Chile. *Tectonophysics*. Retrieved from http://www.sciencedirect.com/science/article/pii/S0040195116301330

Pouya, A., & Ghoreychi, M. (2001). Determination of rock mass strength properties by homogenization. *International Journal for Numerical and*. Retrieved from http://onlinelibrary.wiley.com/doi/10.1002/nag.176/full

Provost, A., Chéry, J., & Hassani, R. (2003). 3D mechanical modeling of the GPS velocity field along the North Anatolian fault. *Earth and Planetary Science Letters*. Retrieved from http://www.sciencedirect.com/science/article/pii/S0012821X03000992

Regenauer-Lieb, K., Hobbs, B., & Ord, A. (2004). On the thermodynamics of listric faults. *Earth, Planets and Space*. Retrieved from https://www.jstage.jst.go.jp/article/eps1998/56/12/56_12_1111/_article/-char/ja/

Regenauer-Lieb, K., & Yuen, D. (2003). Modeling shear zones in geological and planetary sciences: solid-and fluid-thermal–mechanical approaches. *Earth-Science Reviews*. Retrieved from http://www.sciencedirect.com/science/article/pii/S0012825203000382

Regenauer-Lieb, K., & Yuen, D. (1998). Rapid conversion of elastic energy into plastic shear heating during incipient necking of the lithosphere. *Geophysical Research Letters*. Retrieved from http://onlinelibrary.wiley.com/doi/10.1029/98GL02056/full

Riedel, W. (1929). Zur mechanik geologischer brucherscheinungen. *Für Mineralogie,*

Geologie Und Paläontologie B.

Ritz, J. (1994). Determining the slip vector by graphical construction: use of a simplified representation of the stress tensor. *Journal of Structural Geology*. Retrieved from http://www.sciencedirect.com/science/article/pii/0191814194901244

Roman, D., & Cashman, K. (2006). The origin of volcano-tectonic earthquake swarms. *Geology*. Retrieved from http://geology.gsapubs.org/content/34/6/457.short

Roquer, T., Arancibia, G., Rowland, J., Iturrieta, P., Morata, D., & Cembrano, J. (2017). Fault-controlled development of shallow hydrothermal systems: Structural and mineralogical insights from the Southern Andes. *Geothermics*, *66*. https://doi.org/10.1016/j.geothermics.2016.12.003

Rosenau, M., Melnick, D., & Echtler, H. (2006). Kinematic constraints on intra-arc shear and strain partitioning in the southern Andes between 38°S and 42°S latitude. *Tectonics*, *25*(4), n/a-n/a. https://doi.org/10.1029/2005TC001943

Rubin, A. M. (1993). Dikes vs. diapirs in viscoelastic rock. *Earth and Planetary Science Letters*, *117*(3–4), 653–670. https://doi.org/10.1016/0012-821X(93)90109-M

Rubin, A. M. (1995). Propagation of Magma-Filled Cracks. *Annual Review of Earth and Planetary Sciences*, *23*(1), 287–336. https://doi.org/10.1146/annurev.ea.23.050195.001443

Russo, R., Gallego, A., & Comte, D. (2011). Triggered seismic activity in the Liquiñe-Ofqui fault zone, southern Chile, during the 2007 Aysen seismic swarm. *Geophysical*. Retrieved from http://gji.oxfordjournals.org/content/184/3/1317.short

Sanchez-Alfaro, P., Sielfeld, G., Campen, B. Van, Dobson, P., Fuentes, V., Reed, A., … Morata, D. (2015). Geothermal barriers, policies and economics in Chile – Lessons for

the Andes. *Renewable and Sustainable Energy Reviews*, *51*, 1390–1401. https://doi.org/10.1016/j.rser.2015.07.001

Sánchez, P., Pérez-Flores, P., Arancibia, G., Cembrano, J., & Reich, M. (2013). Crustal deformation effects on the chemical evolution of geothermal systems: the intra-arc Liquiñe–Ofqui fault system, Southern Andes. *International Geology Review*, *55*(11), 1384–1400. https://doi.org/10.1080/00206814.2013.775731

Schmalholz, S., & Maeder, X. (2012). Pinch-and-swell structure and shear zones in viscoplastic layers. *Journal of Structural Geology*. Retrieved from http://www.sciencedirect.com/science/article/pii/S0191814112000351

Scholz, C. (1988). The brittle-plastic transition and the depth of seismic faulting. *Geologische Rundschau*, *77*(1), 319–328. https://doi.org/10.1007/BF01848693

Scholz, C. (2002). *The mechanics of earthquakes and faulting*. Retrieved from https://books.google.cl/books?hl=en&lr=&id=JL1VM5wMbrQC&oi=fnd&pg=PR11&dq=The+mechanics+of+earthquakes+and+faulting&ots=tElZYA7qZD&sig=NTdvNDKAUGou3fRiKXSh4_1hLPs

Schueller, S., Gueydan, F., & Davy, P. (2005). Brittle-ductile coupling: Role of ductile viscosity on brittle fracturing. *Geophysical Research*. Retrieved from http://onlinelibrary.wiley.com/doi/10.1029/2004GL022272/full

Secor, D. (1965). Role of fluid pressure in jointing. *American Journal of Science*. Retrieved from http://www.ajsonline.org/content/263/8/633.short

Segall, P., & Simpson, C. (1986). Nucleation of ductile shear zones on dilatant fractures. *Geology*. Retrieved from http://geology.gsapubs.org/content/14/1/56.short

Sibson, R. (1992). Fault-valve behavior and the hydrostatic-lithostatic fluid pressure

interface. *Earth-Science Reviews*. Retrieved from http://www.sciencedirect.com/science /article/pii/001282529290019P

Sibson, R. (1994). Crustal stress, faulting and fluid flow. *Geological Society, London, Special Publications*.

Sibson, R. (2004). Controls on maximum fluid overpressure defining conditions for mesozonal mineralisation. *Journal of Structural Geology*. Retrieved from http://www.sciencedirect.com/science/article/pii/S0191814103001743

Sibson, R., & Moore, J. (1975). Seismic pumping—a hydrothermal fluid transport mechanism. *Journal of the Geological*. Retrieved from http://jgs.lyellcollection.org/content/131/6/653.short

Sielfeld, G., Cembrano, J., & Lara, L. (2016). Transtension driving volcano-edifice anatomy: Insights from Andean transverse-to-the-orogen tectonic domains. *Quaternary International*. Retrieved from http://www.sciencedirect.com/science/article/pii /S1040618215301051

Stanton-Yonge, A. (2016). *Tectonic role of margin-parallel and margin-transverse faults during oblique subduction at the southern volcanic zone of the Andes (master's thesis)*. *Pontificia Universidad Católica de Chile*. Retrieved from https://repositorio.uc.cl/ handle/11534/16840

Tardani, D., Reich, M., Roulleau, E., & Takahata, N. (2016). Exploring the structural controls on helium, nitrogen and carbon isotope signatures in hydrothermal fluids along an intra-arc fault system. *Et Cosmochimica Acta*. Retrieved from http://www.sciencedirect.com/science/article/pii/S0016703716302009

Tchalenko, J. (1970). Similarities between shear zones of different magnitudes. *Geological Society of America Bulletin*. Retrieved from http://gsabulletin.gsapubs.org

/content/81/6/1625.short

Teyssier, C., Tikoff, B., & Markley, M. (1995). Oblique plate motion and continental tectonics. *Geology*, *23*(5), 447–450. https://doi.org/10.1130/0091-7613(1995)023<0447:OPMACT>2.3.CO;2

Thomson, S. N. (2002). Late Cenozoic geomorphic and tectonic evolution of the Patagonian Andes Late Cenozoic geomorphic and tectonic evolution of the Patagonian Andes between latitudes 42 Њ S and 46 Њ S : An appraisal based on fission-track results from the transpressional intr. *Geological Society of America Bulletin*, *114*(9), 1159–1173. https://doi.org/10.1130/0016-7606(2002)114<1159

Tibaldi, A. (1995). Morphology of pyroclastic cones and tectonics. *Journal of Geophysical Research: Solid Earth*. Retrieved from http://onlinelibrary.wiley.com/doi/10.1029/95JB02250/full

Tikoff, B., & Teyssier, C. (1994). Strain modeling of displacement-field partitioning in transpressional orogens. *Journal of Structural Geology*, *16*(11), 1575–1588. https://doi.org/10.1016/0191-8141(94)90034-5

Tullis, J., & Yund, R. (1987). Transition from cataclastic flow to dislocation creep of feldspar: mechanisms and microstructures. *Geology*. Retrieved from http://geology.gsapubs.org/content/15/7/606.short

Vargas, G., Rebolledo, S., Sepúlveda, S., & Lahsen, A. (2013). Submarine earthquake rupture, active faulting and volcanism along the major Liquiñe-Ofqui Fault Zone and implications for seismic hazard assessment in the. *Andean*. Retrieved from http://www.redalyc.org/html/1739/173925397007/

Voce, E. (1955). A practical strain-hardening function. *Metallurgia*.

Wang, K., Hu, Y., Bevis, M., Kendrick, E., Smalley, R., Vargas, R. B., & Lauría, E. (2007). Crustal motion in the zone of the 1960 Chile earthquake: Detangling earthquake-cycle deformation and forearc-sliver translation. *Geochemistry, Geophysics, Geosystems*, *8*(10), n/a-n/a. https://doi.org/10.1029/2007GC001721

White, S. H., Burrows, S. E., Carreras, J., Shaw, N. D., & Humphreys, F. J. (1980). On mylonites in ductile shear zones. *Journal of Structural Geology*, *2*(1–2), 175–187. https://doi.org/10.1016/0191-8141(80)90048-6

Wicks, C., Llera, J. de La, Lara, L., & Lowenstern, J. (2011). The role of dyking and fault control in the rapid onset of eruption at Chaitén volcano, Chile. *Nature*. Retrieved from http://www.nature.com/nature/journal/v478/n7369/abs/nature10541.html

Woodcock, N. H., & Fischer, M. (1986). Strike-slip duplexes. *Journal of Structural Geology*, *8*(7), 725–735. https://doi.org/10.1016/0191-8141(86)90021-0

Zienkiewicz, O., & Taylor, R. (2000a). *The finite element method: solid mechanics*. Retrieved from https://books.google.cl/books?hl=en&lr=&id=MhgBfMWFVHUC&oi=fnd&pg=PR13&dq=ZIENKIEWICZ&ots=2Qm7fxXzbw&sig=t-ohfs-8sbPAOXSdW2RsD7plVME

Zoback, M. D., & Healy, J. H. (1992). In situ stress measurements to 3.5 km depth in the Cajon Pass Scientific Research Borehole: Implications for the mechanics of crustal faulting. *Journal of Geophysical Research*, *97*(B4), 5039. https://doi.org/10.1029/91JB02175